Meteorologische Zeitschrift, Vol. 23, No. 4, 349–368 (published online August 27, 2014)

Entrainment and mixing at the interface of shallow cumulus clouds: Results from a combination of observations and simulations

Fabian Hoffmann[1*], Holger Siebert[2], Jörg Schumacher[3], Theres Riechelmann[1], Jeannine Katzwinkel[2], Bipin Kumar[3,4], Paul Götzfried[3] and Siegfried Raasch[1]

[1]Institute of Meteorology and Climatology, Leibniz Universität Hannover, Germany
[2]Leibniz Institute for Tropospheric Research, Leipzig, Germany
[3]Institute of Thermodynamics and Fluid Mechanics, Ilmenau University of Technology, Germany
[4]Present address: Indian Institute of Tropical Meteorology, Pune, Maharashtra, India

(Manuscript received February 28, 2014; in revised form May 28, 2014; accepted June 4, 2014)

Abstract

This study combines observations, large-eddy simulations (LES), and direct numerical simulations (DNS) in order to analyze entrainment and mixing in shallow cumulus clouds at all relevant spatial scales and, additionally, to verify the results by the multiple methods used. The observations are based on three flights of the CARRIBA campaign which are similar to the classical BOMEX case used for LES. Virtual flights in the LES data are used to validate the observational method of line measurements. It is shown that line measurements overrepresent the cloud core, and it is quantified how derived statistics depend on small perturbations of the flight track, which has to be taken in account for the interpretation of airborne observations. A linear relation between fluctuations of temperature and liquid water content has been found in both LES and observations in a good quantitative agreement. However, the constant of proportionality deviates from purely adiabatic estimates, which can be attributed to cloud edge mixing. The cloud edge is compared in detail in observations and LES, which agree qualitatively although the LES cloud edge is smoother due to the model's resolution. The resulting typical amplitudes of the turbulence fields from this comparison are compared with the large-scale forcing model which is used in a series of DNS which study the mixing below the meter scale, which show that LES does not resolve the intermittency of small-scale turbulence.

Keywords: cumulus clouds, airborne observations, large-eddy simulations, direct numerical simulations, entrainment and mixing

1 Introduction

Shallow cumulus clouds are ubiquitous in the trade-wind regions. They play an important role in the moisture transport to the free atmosphere (Tiedtke, 1989), and for the Earth's radiation budget (Albrecht et al., 1995). Furthermore, shallow cumulus convection significantly influences the dynamics of the entire planetary boundary layer by intensifying the vertical transport of moisture, momentum, and heat from the surface to higher levels. In addition, trade-wind cumuli buffer the interaction between the ocean surface and the free atmosphere (Siebesma et al., 2003). The size distribution, the shape and the lifetime of cumuli is determined by turbulent entrainment processes in which clear environmental air is mixed with cloudy air.

Trade-wind regions are considered as one of the best natural laboratories for warm shallow cumulus clouds because the meteorological conditions are quite stable which allows for statistically significant cloud sampling under similar conditions. Therefore, many landmark papers (e. g., Malkus, 1954, 1956 1958) with different aspects of shallow cumulus convection are based on observations made in this area. Although much progress has been made during the last five decades by observations and simulations, our understanding of cumulus clouds is still limited. Clouds incorporate physical processes which span over at least five orders of magnitude in space (and time) ranging from the cloud's macrostructure $\mathcal{O}(10^2\,\mathrm{m})$ to their microscale $\mathcal{O}(10^{-3}\,\mathrm{m})$, and many interactions and feedbacks of these scales are still poorly understood. Therefore, all approaches lack of a comprehensive representation of all relevant scales. For example, airborne measurements resolve cumulus convection from its macrostructure down to 15 cm using slowly-cruising helicopters (Siebert et al., 2006b) but are limited to one-dimensional time series (e. g., Heus et al., 2009). Large-eddy simulations (LES) of single evolving clouds started with two-dimensional approaches such as in Grabowski (1989). Present state-of-the-art LES resolve the three-dimensional macrostructure of the cloud but are still limited by the smallest resolvable scales at $\mathcal{O}(10\,\mathrm{m})$ (e. g., Matheou et al., 2011). Finally,

*Corresponding author: Fabian Hoffmann, Leibniz Universität Hannover, Germany, e-mail: hoffmann@muk.uni-hannover.de

DOI 10.1127/0941-2948/2014/0597
Gebrüder Borntraeger Science Publishers, Stuttgart, www.borntraeger-cramer.com

direct numerical simulations (DNS) fully resolve the clouds microstructure down to the Kolmogorov length $\left(\mathcal{O}(10^{-3}\,\mathrm{m})\right)$ but their largest resolvable scales are limited to $\mathcal{O}(10^{0}\,\mathrm{m})$ (e. g., Abma et al., 2013; Kumar et al., 2012, 2013, 2014). As a consequence, these studies are still limited to homogeneous mixing or the transition to inhomogeneous mixing. Thus a combination of different investigation methods is one strategy to cover all relevant scales and to understand each method's limitations. This sets the stage for our joint effort.

In the present work, we want to take a first step in this direction and combine cloud observations, LES, and DNS to study all relevant scales of cumulus convection with a focus on the entrainment and mixing dynamics, but also the shortcomings of each approach by validating their results by each other. Furthermore, we would like to discuss some consequences which arise from a coarse resolution or sampling of turbulence properties for the small-scale fluctuations. The observational basis for our study are data records from the CARRIBA (**C**loud, **A**erosol, **R**adiation and tu**R**bulence in the trade w**I**nd regime over **BA**rbados) campaign, a project based on two one-month field studies in November 2010 and April 2011 over Barbados (Siebert et al., 2013). The main focus of CARRIBA were comprehensive aerosol, cloud, radiation, and cloud turbulence observations with the helicopter-borne payloads ACTOS (**A**irborne **C**loud **T**urbulence **O**bservation **S**ystem). One highlight of these observations is the high spatial resolution of decimeter-scale or below which allows for analyzing the fine-scale structure of individual clouds (e. g., Katzwinkel et al., accepted). The data of the CARRIBA campaign provide thus also a state-of-the-art data base of the cloud-clear air interface.

For the initialization of our LES studies, we used a setup proposed by Siebesma et al. (2003), which is based on generalized observations of the comprehensive field study "**B**arbados **O**ceanographic and **M**eteorological **EX**periment" (BOMEX, Davidson, 1968; Holland and Rasmusson, 1973). Note that we will refer to this LES case as BOMEX in the following. Three CARRIBA data sets in the period April 13 to 14, 2011 with similar stratification as BOMEX have been considered as the observational background for this study. Within the LES which are calculated by the model PALM (Raasch and Schröter, 2001) several virtual ACTOS-like flight tracks are simulated. This allows a direct comparison of data gained from real ACTOS flights during CARRIBA and virtual flights in the LES domain. First, the basic background conditions in terms of general stratification are analyzed and compared. One specific question in this context concerns the sampling of individual clouds and how well the estimated averages describe the cloud ensemble. In this context, it should be considered that typical cloud observations consist of a single one-dimensional cloud penetration from which mean parameters such as liquid water content or others are derived, that is, line averages are interpreted as mean cloud parameters for a given height. The typical small cloud diameter and rapid development of these cloud types did not allow to penetrate the same cloud more than one time. Besides validating airborne observations by LES, our study investigates fluctuations of temperature and liquid water content (LWC) in both CARRIBA and virtual BOMEX flights. These fluctuations are caused by the interfacial entrainment of cloud-free air and the subsequent mixing resulting in the evaporation of cloud droplets and the corresponding cooling of air (e. g., Gerber et al., 2008). This mixing process increases buoyancy driven downdrafts at the cloud edge, the so-called subsiding shell, and hence the turbulent dissipation (e. g., Siebert et al., 2006a, Heus and Jonker, 2008). This highly turbulent region cannot be sufficiently resolved by LES due to their comparably large grid spacing. The ranges of scales which have to be bridged between the LES of a whole cloud and DNS which incorporate the cloud water droplet dynamics and microphysics is still too big. In a first step, we will therefore report here DNS studies which aim at understanding the impact of unresolved subgrid scales on central quantities such as increment moments of the turbulent velocity fields. Our approach will be based on conditioning the velocity increment statistics to high-dissipation events.

This paper is structured as follows. The next Sec. 2 describes the observational system ACTOS as well as the LES and DNS models used for this study (Sec. 2.1–2.3). The section closes with a comparison of virtual airborne measurements carried out in the BOMEX LES and three flights of the CARRIBA campaign (Sec. 2.4) assuring the comparability of simulations and observations used in the following. Fluctuations of temperature and liquid water content in the BOMEX case and the CARRIBA campaign are compared in Sec. 3, while the representativeness of airborne measurements is analyzed in Sec. 4. The interface of a shallow cumulus cloud, i. e., the cloud edge, in observations and LES is analyzed in Sec. 5, which prepares the DNS presented in Sec. 6, which have been driven and sustained in a statistically stationary regime by typical values of variables at the cloud edge obtained by LES. This paper concludes with a summary and a short discussion (Sec. 7).

2 Experiments and simulations

2.1 The Airborne Cloud Turbulence Observation System ACTOS

ACTOS is an autonomous payload for high resolution in-situ measurements in warm boundary layer clouds. The payload is carried as external cargo about 170 m below a helicopter. The long rope allows the ACTOS to be dipped into the cloud while the helicopter remains above the cloud for safety reason. Furthermore, the long rope

results in stable flight conditions with only a smooth pendulum motion with a time period of approx. 25 s. In combination with a typical true airspeed of 20 m s^{-1} no influence of the helicopter rotor downwash is visible in the data and the spatial resolution of the measurements is on the order of 10 cm. In this study we mainly focus on observations of the following parameter: i) three-dimensional wind velocity vector (u, v, w) measured with an ultrasonic anemometer (Siebert and Muschinski, 2001) which is corrected for payload altitude and motion, ii) temperature T which is observed by an fine-wire resistance thermometer protected for cloud droplet impaction (Haman and Malinowski, 1996), and iii) the mixing ratios of water vapor q_v based on an infra-red absorption hygrometer, and liquid water q_l with the particle volume monitor PVM-100A (Gerber et al., 1994). A comprehensive overview of ACTOS including a detailed description of its devices can be found in Siebert et al. (2006b).

2.2 The large-eddy simulation model PALM

The LES model used for this study is PALM[1] (Raasch and Schröter, 2001; Riechelmann et al., 2012), which has been widely applied to study different flow regimes, including the convective boundary layer (e. g., Raasch and Franke, 2011), and to simulate virtual flights (e. g., Schröter et al., 2000; Sühring and Raasch, 2013). PALM solves the filtered, non-hydrostatic, Boussinesq approximated Navier-Stokes equations. A prognostic equation for the subgrid scale turbulent kinetic energy is solved applying the sub-grid scale closure model by Deardorff (1980). Using finite differences, a fifth-order advection scheme (Wicker and Skamarock, 2002) and a third-order Runge-Kutta time step scheme are applied. For the simulation of clouds, prognostic equations for the liquid water potential temperature and the total water specific humidity are solved. The liquid water content is diagnosed by saturation adjustment, i. e., a grid volume is either regarded as unsaturated when the total water content is below the saturation value or as saturated otherwise (Cuijpers and Duynkerke, 1993). Some details about the present setup of PALM are given in Sec. 2.4.1.

2.3 The direct numerical simulation model

DNS resolve all dynamically relevant scales in a turbulent flow and make no use of a subgrid scale model. It is clear that DNS can monitor therefore the turbulent evolution in a small sub volume of the cloud only. The typical box size does not exceed much more than a meter given that the typical Kolmogorov length $\eta_K \sim 1$ mm. In the present work, we will focus here on the case of pure hydrodynamic aspects and exclude the dynamics of vapor and temperature fields for the study which has been analyzed in Kumar et al. (2012, 2013, 2014). Reasons for this step will be given in Sec. 6. Numerically we apply a pseudospectral method and solve the equations of motions in a cubic volume with periodic boundary conditions in all three directions. All fields are expanded in Fourier series and this enables the usage of fast Fourier transforms which are parallelized in two space dimensions and result in a domain decomposition into pencils. The simulation program is parallelized using MPI (message passing interface). The time stepping is done here by a second-order predictor-corrector method. More details on the volume forcing of the bulk turbulence can be found in Kumar et al. (2013) or Schumacher et al. (2007).

2.4 Comparison of BOMEX simulations and CARRIBA observations

2.4.1 Setup of BOMEX simulations and retrieval of virtual measurements

The setup of the LES simulation follows closely those of the BOMEX (Barbados Oceanographic and Meteorological Experiment) shallow cumulus case from Siebesma et al. (2003). It describes a typical steady-state trade-wind boundary layer which is similar to the conditions of the CARRIBA campaign. They are compared in Sec. 2.4.3. Besides the initial profiles of the temperature and humidity, the setup prescribes an initial profile for the turbulent kinetic energy and the horizontal wind components (eastwind), constant surface fluxes for momentum as well as sensible and latent heat, and large-scale forcing terms like subsidence, radiative cooling and low-level drying (Siebesma et al., 2003). The convection is initially triggered by small random perturbations of the potential temperature and specific humidity fields within the lowest 1600 m. The simulation uses cyclic (also denoted as periodic) lateral boundary conditions.

In contrast to Siebesma et al. (2003), an isotropic grid resolution of $\Delta x \equiv \Delta y \equiv \Delta z = 5$ m instead of 100 m is used for this study. Accordingly, the number of grid points is increased to $1280 \times 1280 \times 610$ resulting in a model domain of 6.4 km $\times$ 6.4 km $\times$ 3.2 km. The smaller grid spacing is chosen because of the comparison with the ACTOS measurements which have a spatial resolution of 15 cm. However, a grid resolution on centimeter scale is not feasible for this study, since the model domain has to be large enough to resolve the corresponding convective scales and to generate a proper number of clouds. Thus a grid resolution of 5 m is chosen as a compromise.

The LES simulations are used to perform virtual flights through the domain of calculated data mimicking the ACTOS tracks in order to compare these data to the corresponding three-dimensional data. Since we are not able to change the virtual flight pattern during the simulation, i. e., reacting on the cloud field (like a pilot does), we performed two identical simulations from which the first one is used to identify the clouds and to generate

[1] at revision 1116, http://palm.muk.uni-hannover.de/browser?rev=1116

a flight pattern, which is used in the second simulation for the virtual measurements. Thereby the flight pattern closely follows those of ACTOS: it crosses the center of the cloud $\sim$ 100 m below the cloud top with a horizontal true air speed of $\sim 20\,\mathrm{m\,s^{-1}}$ and a climb rate of $5\,\mathrm{m\,s^{-1}}$. Contrary to real ACTOS, the virtual airplane is placed in front of a new cloud immediately after it left the previous one. The virtual measurements are taken at every time step ($\sim$ 0.38 s) and record the potential temperature, the humidity, the LWC, the dissipation rate, and the wind velocity components. Two flight patterns are simulated simultaneously capturing $\sim$ 74 clouds during a time span of 500 s. Each flight pattern is analyzed by four airplanes: one on the proposed track and the remainder locally shifted by 20 m to the left, right or down, respectively, for studying the impact of the flight path on the retrieved cloud statistics (see Sec. 4). The virtual airplane measurements are performed after the spin-up phase of two hours.

Besides the virtual cloud tracking measurements further flights crossing the boundary layer vertically (0–2500 m and 2500–0 m) were performed. These virtual airplanes were headed in north-east direction (angle of 20 °), in order to avoid crossing the same locations within the model domain during their flights due to the cyclic boundary conditions.

2.4.2 Estimate of mean energy dissipation rate in both data sets

The BOMEX data is used to investigate methods usually applied for the real ACTOS data. In this context the method of estimating local energy dissipation rates ε_τ over short sub-record of length τ is applied to our virtual BOMEX flights and compared with the results from the LES sub-grid model (see Deardorff, 1980). The ACTOS values of ε_τ are derived from the second-order structure function (or second-order velocity increment moment) $D_u^\tau(t') = \left\langle (u(t+t') - u(t))^2 \right\rangle_\tau$ with the time lag t' and the longitudinal wind velocity component u. In the inertial subrange the structure function follows the classical Kolmogorov scaling (Frisch, 1995) with $D_u^\tau(t') \propto (t' \langle U \rangle_\tau)^{2/3}$ and it can be shown that

$$\varepsilon_\tau = \left(\frac{1}{2} D_u^\tau(t') \right)^{3/2} / \left(t' \langle U \rangle_\tau \right) \qquad (2.1)$$

with $\langle U \rangle_\tau$ denotes an average of u over the time τ. Fig. 1 shows a 500 s long BOMEX record from a virtual flight in the sub-cloud layer 50 m above sea level. The dotted black line indicates the ε_τ values from the sub-grid model with 5 m resolution which corresponds to the grid spacing of the LES. The symbols represent ε_τ estimated from the second-order structure function calculated from non-overlapping sub-records of a length of 30 samples. Taking the time resolution of the virtual flights of 0.4 s the 30 samples results in an integration time of 12 s. The results of this analysis suggest that the method of estimating ε_τ based on $D_u^\tau(t')$ which is usually applied for real ACTOS flights compares qualitatively with the results from the sub-grid model and both methods reproduce the general structure and amplitudes of ε_τ.

2.4.3 Comparison of vertical profiles between simulation and observation

Three flights performed on April 13 (one flight) and April 14 (two flights) in 2011 have been identified to compare best with the BOMEX case (Fig. 2). These observations are compared in terms of stratification with area-averaged profiles of the BOMEX simulations (labeled with AP) and one virtual flight in the BOMEX domain (labeled with VP) with similar sampling characteristics as the real ACTOS flights. The mean ACTOS profiles are averages over three complete flights including cloud penetrations. This has been done by sorting all measurements of the three flights into height bins over which the average has been calculated. First, vertical profiles of the potential temperature for dry air $\Theta = T\,(p_0/p)^{R_L/c_p}$ are compared in Fig. 2 a. Here, T is the actual temperature, p and p_0 are the actual static pressure and reference pressure at ground, R_L is the gas constant for air, and c_p is the specific heat capacity of air at constant pressure. The slope of Θ compares quite well for heights below 1500 m, although in that height range CARRIBA was about 1 K warmer compared to all BOMEX data. In general, the BOMEX case was characterized by a 500 m thick temperature inversion above 1500 m which was never observed during CARRIBA. The typical trade inversion during CARRIBA was less pronounced and observed at higher levels, often around 2.0 to 2.5 km. However, this difference is less important for our inter-comparison because our CARRIBA cloud observations are bounded to 1500 to 1800 m and are, therefore, only slightly higher compared to the BOMEX clouds limited in height by the inversion in 1500 m. The same arguments hold for the moisture profile (Fig. 2 b) which agrees also quantitatively for heights below 1200 m. For higher levels the BOMEX case is drier due to the large scale subsidence and the capping inversion layer. Fig. 2 c shows a combination of all observations of q_l for all of the three CARRIBA flights as a function of height. These data should not be misinterpreted as a vertical profile through a single cloud. A dot-dashed line represents the adiabatic liquid water mixing ratio which is an upper bound for the observations. As a result of the constant sea surface temperature and, therefore, a similar cloud base observed in 500 m the adiabatic profiles are almost the same for all three CARRIBA data and the BOMEX case. Due to lateral entrainment the difference between observation and the adiabatic value increases with height which is a typical feature. For one profile of BOMEX (labeled as VP) a short cloud penetration is obvious with similar values of q_l compared to the CARRIBA data.

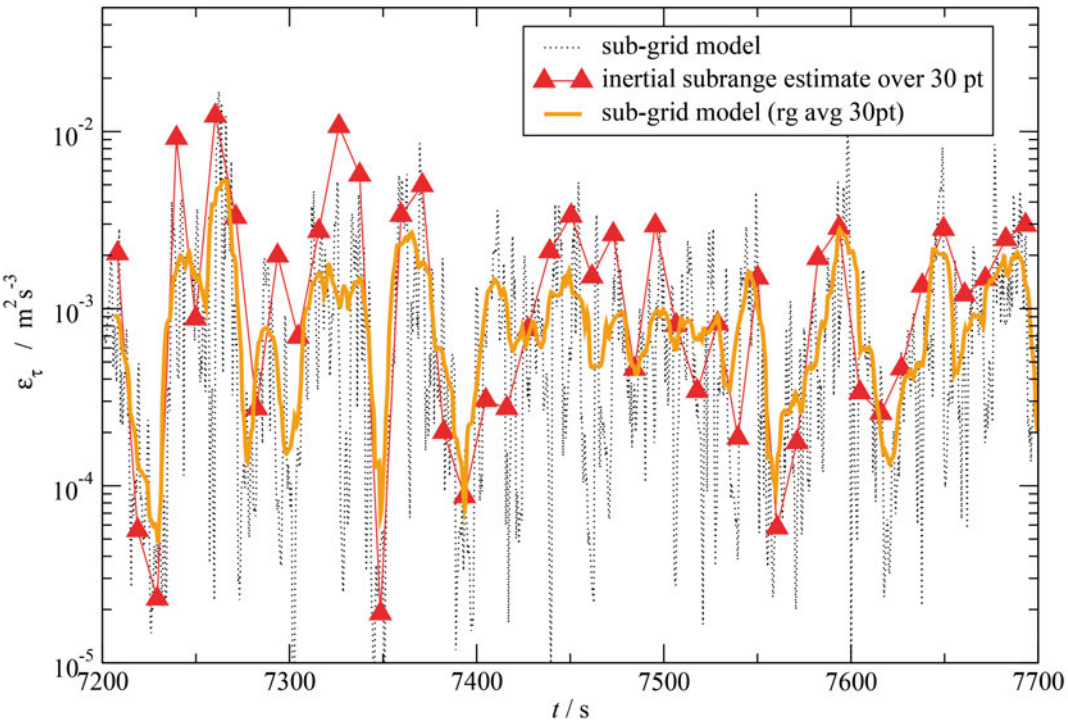

Figure 1: Local energy dissipation rate in $m^2\,s^{-3}$ as a function of time in s estimated by (i) the LES sub-grid model non-averaged (dotted black line) and applying a 30 point running average (orange line), and by (ii) the second-order structure function D_u^τ of the longitudinal wind velocity u (red symbols). Data are gathered from virtual BOMEX flight in the sub-cloud layer in 50 m above sea level.

Fig. 2 d shows the profiles of ε (cf. Sec. 2.4) as a measure for the local degree of turbulence. There is a quantitative agreement of the averaged CARRIBA observations with the area-averaged BOMEX data (AP) for the sub-cloud layer. Above 500 m the CARRIBA data are slightly higher compared with the BOMEX profile AP. This is most probably caused by a different number of cloud penetrations which are usually characterized by a several order of magnitude higher degree of turbulence. One single profile of a virtual flight (VP) illustrates the significant difference between turbulence in the conditional unstable area (with $\varepsilon < 10^{-6}\,m^2\,s^{-3}$) and for cloud penetrations (with $\varepsilon \sim 10^{-2}\,m^2\,s^{-3}$). Above the cloud layer, e. g., in the range of the stably stratified inversion layer, the profile of the average ε drops off because only a few clouds are able to penetrate into this stable layers.

3 Correlation of temperature and liquid water content fluctuations

After verifying that the mean vertical profiles can be compared consistently, we focus to the turbulent fluctuations in the following. Previous LES results of stratocumulus clouds (DE ROODE and LOS, 2008) suggest a linear relationship in the form of $T' = c_{q_t'T'} q_t'$ between fluctuations of in-cloud temperature (T') and total water mixing ratio $q_t' = q_v' + q_l'$ with q_v' and q_l' are the mixing ratios of water vapor and liquid water, respectively.

Water vapor fluctuations in the vicinity of cloud droplets are difficult to measure with our instrumentation. We therefore substitute q_v' with the saturation value $q_s'(T) = \frac{dq_s}{dT} T' = \gamma T'$ which yields a new expression for the temperature fluctuations as a linear function of liquid water mixing ratio fluctuations which can be more easily measured (c. f. Eq. 5 in DE ROODE and LOS, 2008):

$$T' = c_{q_l'T'} q_l', \tag{3.1}$$

with $c_{q_l'T'} = c_{q_t'T'} \left(1 - c_{q_t'T'}\gamma\right)^{-1}$.

In Fig. 8 of DE ROODE and LOS (2008) we find for daytime conditions at a mean temperature of 12 °C $c_{q_t'T'} = 723\,K$ which results with $\gamma \approx 0.6\,g\,kg^{-1}\,K^{-1}$ in $c_{q_l'T'} = 1276\,K$ and $c_{q_t'T'} = 1030\,K$ for nighttime which yields $c_{q_l'T'} \approx 2700\,K$.

Next, we investigate if the same simple relationship holds for the CARRIBA and BOMEX flight data in shallow trade wind cumuli (Cu humilis to small

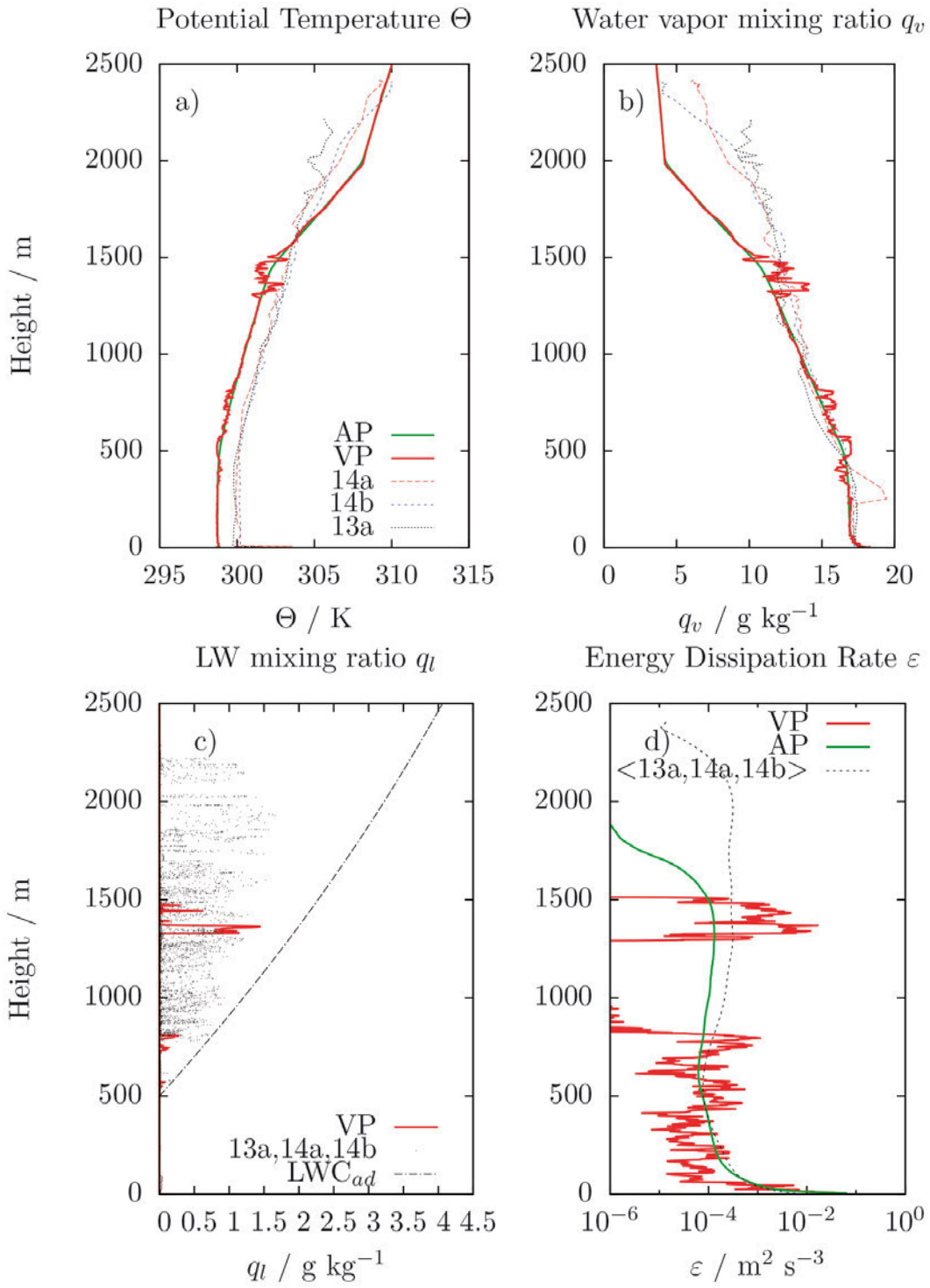

Figure 2: Vertical profiles of (a) potential temperature in K, (b) specific humidity in g kg^{-1}, (c) liquid water mixing ratio in g kg^{-1}, and (d) local energy dissipation rate in m^2 s^{-3} as a function of height above sea level in m for (temporally and horizontally) averaged LES profiles (AP), virtual ACTOS-profiles measured in the LES domain (VP), and averaged ACTOS profiles sampled during three flights (April 13, 14a, and 14b, 2011) of the CARRIBA campaign. The adiabatic liquid water mixing ratio (cloud base at 500 m with $T = 21\,°C$) has been added to (c) for reference. All three CARRIBA profiles (13, 14a, 14b) have been averaged to one profile in (d).

Cu mediocris). For both data sets, a simple cloud detecting algorithm based on a threshold of $q_l = 0.05\,\mathrm{g\,kg^{-1}}$ was applied. In order to increase the statistical significance, the CARRIBA data are based on all three flights and for the BOMEX data several flights at nearly the same height, but horizontally separated by 20 m have been analyzed. The CARRIBA data were averaged to yield the same spatial resolution of 5 m as the BOMEX simulations. With this algorithm about 430 CARRIBA and 237 BOMEX clouds have been collected and ana-

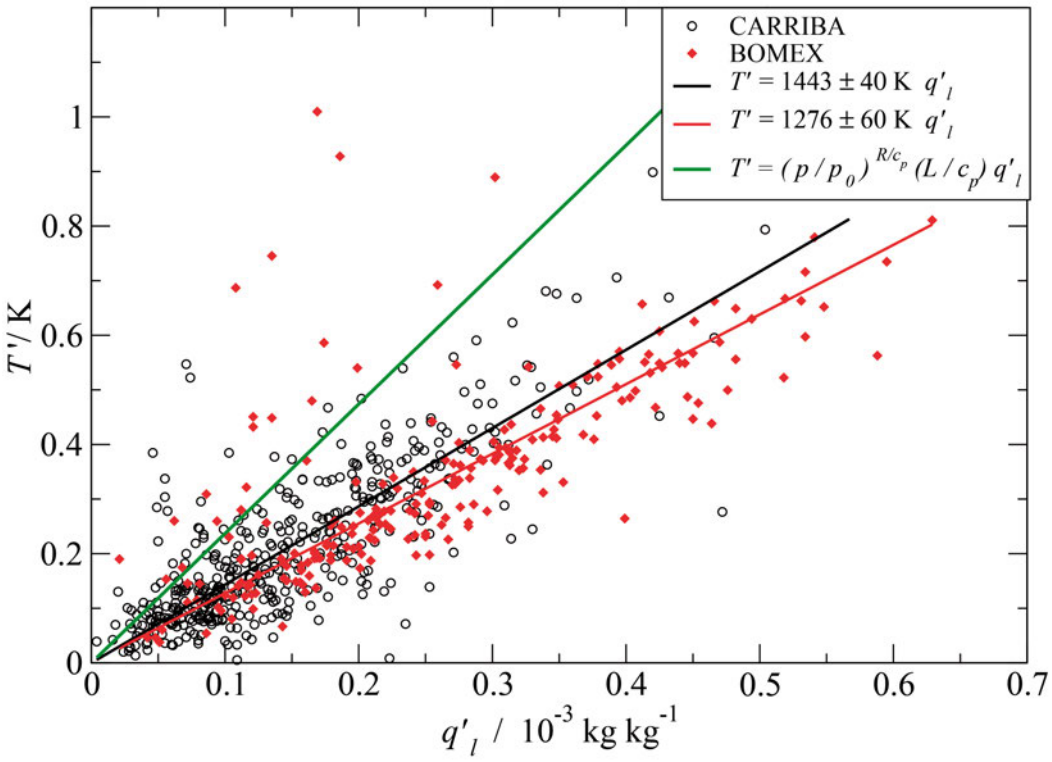

Figure 3: Temperature fluctuations in K as a function of liquid water content fluctuations in 10^{-3} kg kg^{-1} for observations of CARRIBA (black circles), BOMEX-LES (red diamonds), with corresponding linear regressions (black and red lines, respectively), and the adiabatic limit (green line). Only data with a liquid water content > 0.05 g m^{-3} are considered. Each symbol represents a single cloud.

lyzed. For each cloud the variance σ^2 of the liquid water mixing ratio and temperature were estimated and the cloud-averaged fluctuations are defined as $T' = \sigma_T$ and $q'_l = \sigma_{q_l}$, respectively. Fig. 3 shows our result in a scatter plot of $\langle q'_l | T' \rangle$ with each point representing one single cloud. A linear regression yields $c_{q'_l T'} = 1443 \pm 40$ K for the CARRIBA data and $c_{q'_l T'} = 1276 \pm 60$ K for BOMEX. Considering the root-mean-square error of the regression both slopes are in good quantitative agreement.

This simple linear relationship between temperature and liquid water fluctuation is only valid if fluctuations of the liquid water potential temperature $\Theta'_l = \Theta' - \frac{L}{c_p} q'_l$ (Deardorff, 1976) are negligible, that is, the process is purely adiabatic. With this assumption of $\Theta'_l = 0$ an analytical expression for the slope in Eq. 3.1 is found:

$$T' = \left(\frac{p}{p_0}\right)^{R/c_p} \frac{L}{c_p} q'_l. \qquad (3.2)$$

Here, $L = 2.5 \times 10^6$ J kg^{-1} is the latent heat and $c_p = 1004$ J kg^{-1} K^{-1} is the heat capacity of air at constant pressure. For the CARRIBA observations we have a mean pressure level of $p = 850$ hPa and with $p_0 = 1013$ hPa as ground reference we find a slope of 2370 K which is added in Fig. 3 as the adiabatic reference. Most of the data points are below this line, that is, the observed amplitude of liquid water fluctuations results on average in roughly half of the magnitude of the temperature fluctuations. The deviation of the observed $\langle q'_l | T' \rangle$ points from the green line can be taken as a measure of the departure from the adiabatic assumption of $\Theta'_l = 0$ due to mixing with non-cloud air. This deviation might be explained by droplets which experience mixing at cloud edge with droplet-free but almost saturated air from the environment. Such a mixing event would – at least partly – result in a dilution which creates fluctuations in q_l but due to incomplete evaporation the release of latent heat and, therefore, the temperature fluctuations are smaller than predicted by Eq. 3.2. Humid shells around shallow trade-wind cumuli are a frequently observed phenomenon, which is supposed to influence the mixing at cloud edge (Gerber et al., 2008), and can explain the reduced factor $c_{q'_l T'}$. They are also known from large-eddy simulations, e.g. by Heus and Jonker (2008).

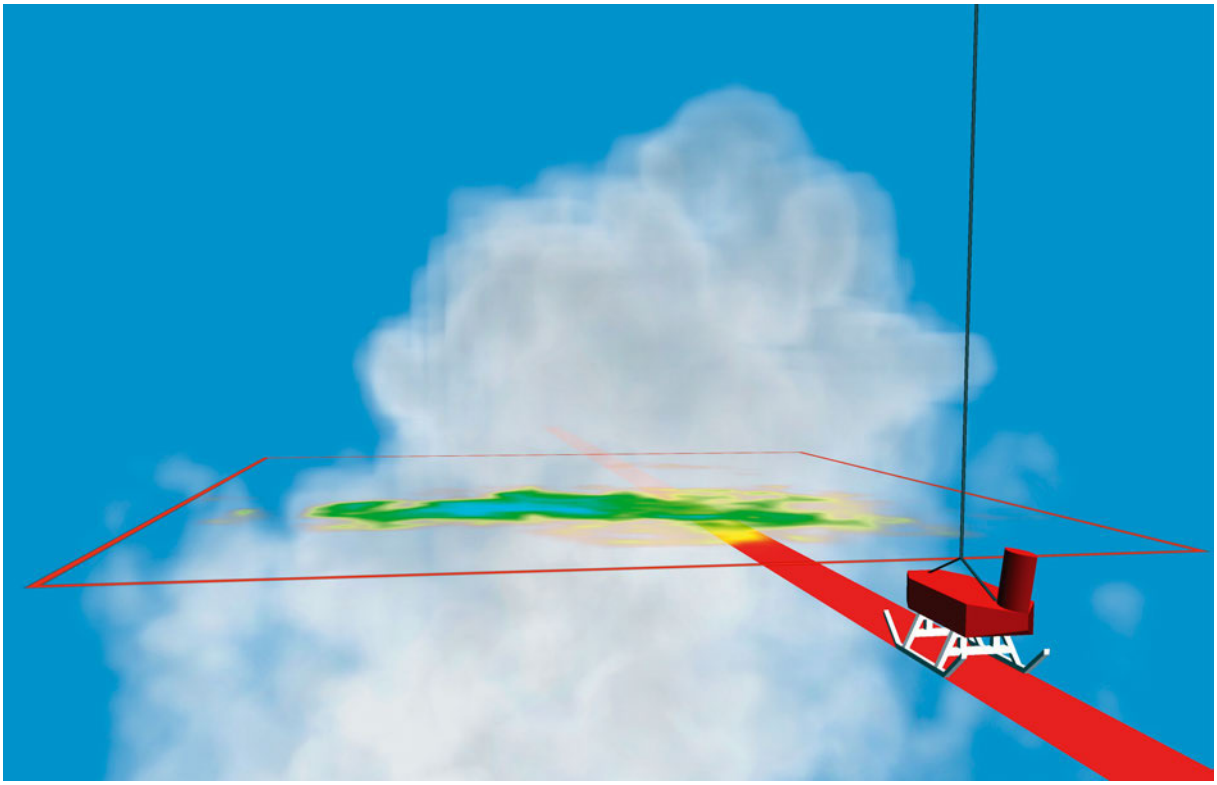

Figure 4: Visualization of virtual ACTOS measurements (broad red line). Gray shaded volumes indicate a positive liquid water content, i. e., a cloud. Inside the red square, a horizontal cross section with contours of the liquid water content at the height of the virtual airplane is displayed. This cross section represents the two-dimensional set of data to which virtual ACTOS measurements are compared to. The visualization is carried out with VAPOR (Clyne et al., 2007).

4 How representative are airborne cloud penetrations compared with ensemble properties?

Airplanes represent clouds by one-dimensional line measurements. In order to validate this way of sampling clouds, we compared the virtual airplane measurements of the BOMEX-LES used in the previous sections to all in-cloud data at the height of the virtual airplane (i. e., two-dimensional cross sections) which we expect to represent the range of variables of the cloud more significantly than the line measurements since they represent a broader statistical base (see Fig. 4). These cross sections are gathered once during the transect of the virtual airplane and hence do not depend on time as line measurements do. For the following, the virtual airplane measurements are denoted as one-dimensional, and the cross sections as two-dimensional.

As an example for one examined cloud, Fig. 5 displays the probability density functions (PDFs) of the one-dimensional and two-dimensional sets of LWC (a) and vertical velocities (b). Although the two-dimensional data is gathered only once during the virtual airplane measurements as explained above, Fig. 5 shows that airplane measurements can be interpreted as subset of the two-dimensional data, since both sets represent the same range of values. This is expectable, since the transection of the cloud by the virtual airplane lasts for 20 to 30 s, a time span in which the cloud's statistics are not expected to change significantly.

Systematic differences between the one-dimensional and two-dimensional measurements become visible by taking more values into account. Fig. 6 displays the PDFs of the collected one-dimensional and two-dimensional sets of LWC (a) and vertical velocities (b) for 33 analyzed clouds of the BOMEX-LES containing altogether 758 one-dimensional and 93 869 two-dimensional values. Besides the statistical noise originating from the smaller set of one-dimensional data, the PDFs of both one- and two-dimensional data obey the same shape, which are, however, shifted to larger values of LWCs and vertical velocities in case of one-dimensional data.

This systematic difference is caused by the way a (virtual) airplane transects a cloud: it preferentially flies through the core of the cloud, i. e., the least diluted part of the cloud with the highest LWCs and vertical velocities. One-dimensional measurements overrepresent the center of the cloud, which is visible from simple geometrical arguments schematically shown in Fig. 7. By applying a simple two-cell model representing a radial symmetric shallow cumulus cloud by an undiluted core (blue) and its cloudy surroundings (red), one can easily show that the ratio between space (and hence the number of measurements) covered by the core and the space covered by the core's surrounding is larger in the

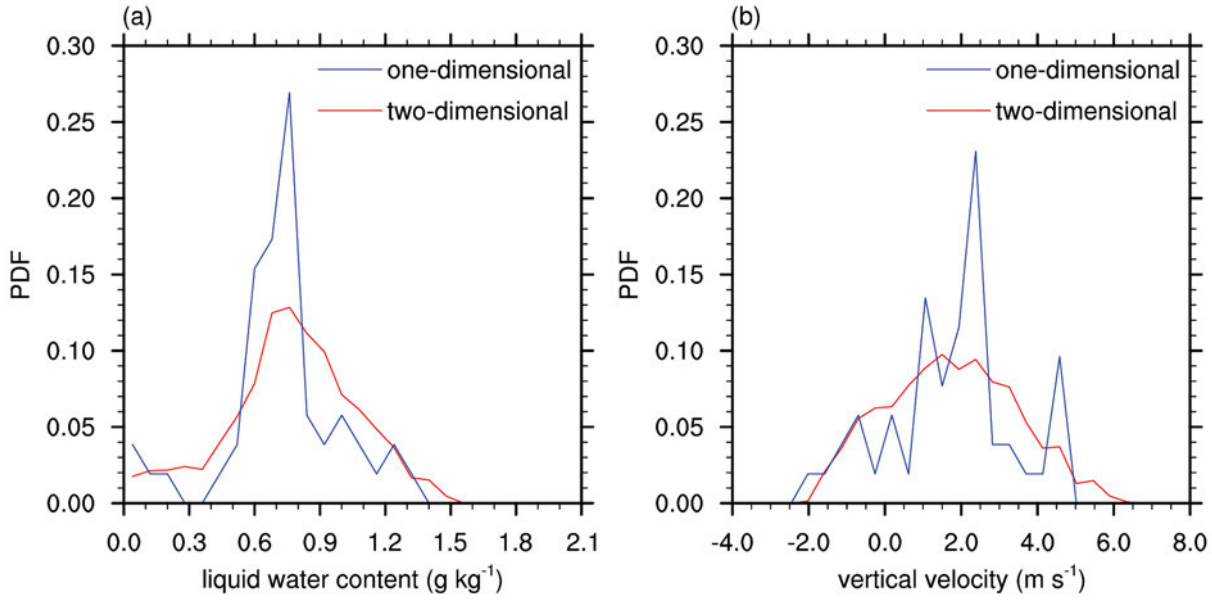

Figure 5: Probability density functions (PDF) for (a) liquid water content in g kg^{-1} and (b) vertical velocity in m s^{-1} for one-dimensional line measurements (blue line) and two-dimensional cross sections (red line) of a single cloud.

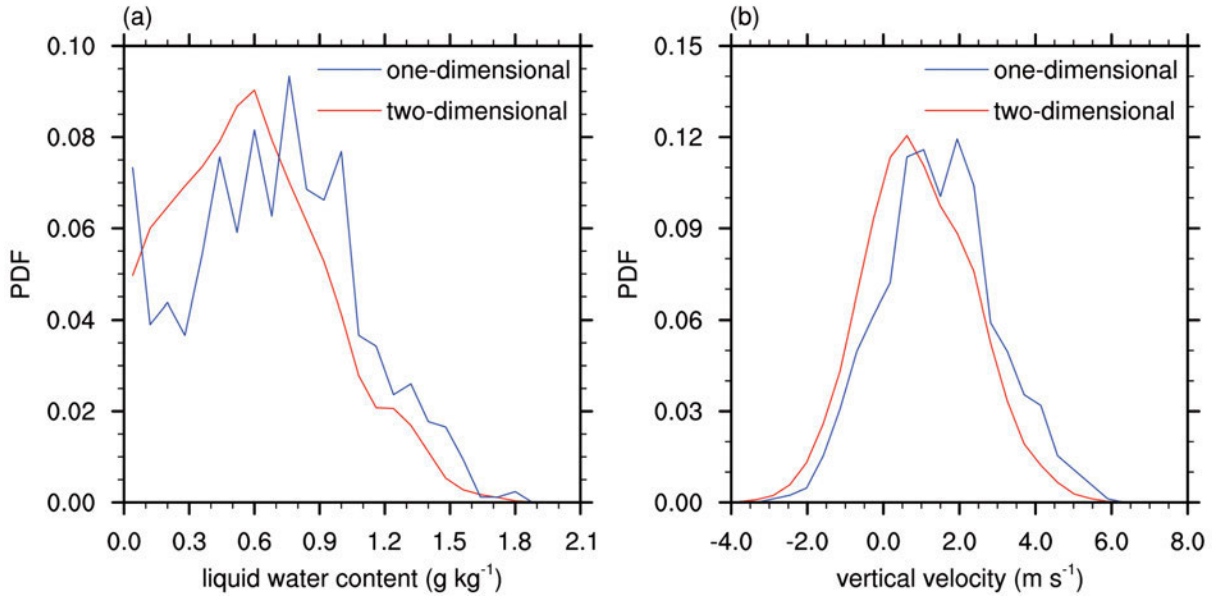

Figure 6: Same as in Fig. 5, but for all 33 analyzed clouds.

one-dimensional χ_{1D} (b) than in the two-dimensional case χ_{2D} (a):

$$\chi_{1D} = \frac{2r_2}{2(r_1 - r_2)} > \frac{\pi r_2^2}{\pi(r_1^2 - r_2^2)} = \chi_{2D}, \qquad (4.1)$$

where $r_1 > r_2 > 0$ are the distances defined in Fig. 7. Thus, properties of the cloud core are overrepresented by one-dimensional measurements resulting in larger vertical velocities and LWCs in comparison to two-dimensional measurements as shown in Fig. 6.

As any other observation, airplane observations are limited by the practicable number of measurements. Therefore, it is necessary to define a confidence interval which allows us to quantify the reliability of our derived statistics, e. g., mean and standard deviation of LWC and vertical velocity as displayed in Fig. 8 (a) and (b). Although theoretical estimates for the confidence interval of mean and standard deviation exist (cf. Chap. 5.4, Von Storch and Zwiers, 2001), assumptions made for their deviation are not valid for our analyzed clouds, e. g., the clouds are part of the same cloud field and hence not statistically independent.

To derive this confidence interval, we evaluate the same virtual flights in the BOMEX-LES as above. Since clouds are examined at different heights, we normalized the one-dimensional line measurements by the arith-

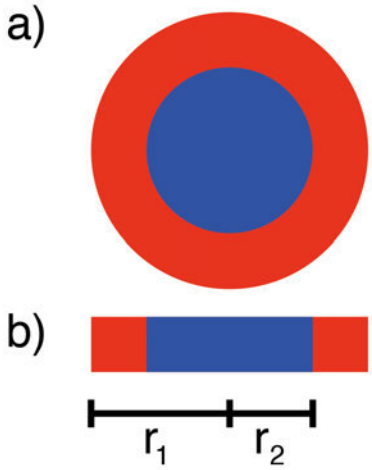

Figure 7: Sketch of a horizontal, two-dimensional (a), and a one-dimensional (b) representation of a cumulus cloud. It consists of a two-cell structure and contains a core (blue) and surrounding values (red). Radii $r_1 > r_2 > 0$ represent measures of length describing the decomposition of the cloud into the two subsets.

metic mean of the corresponding two-dimensional cross sections (see above) making these quantities independent of height:

$$\widehat{\Phi^N_{1D}} = \frac{\Phi^N_{1D}}{E(\Phi^N_{2D})}, \tag{4.2}$$

where, for a given cloud N, Φ^N_{1D} terms the set of data, i. e., the set of all recorded values for a certain variable, gathered by one-dimensional line measurements, and Φ^N_{2D} the corresponding set of two-dimensional data gained from cross sections. E terms the arithmetic mean. Then, we represent our cloud field by a superset of all $M = 33$ analyzed clouds

$$\left\{\widehat{\Phi^1_{1D}}, \widehat{\Phi^2_{1D}}, \ldots, \widehat{\Phi^M_{1D}}\right\}, \tag{4.3}$$

from which we compute mean and standard deviation by taking all recorded values from all clouds into account. By restricting the computation of mean and standard deviation to a lower number of clouds, we quantify the dependence of the confidence interval on the number of measurements displayed in Fig. 8 a and b, respectively. Note that we analyzed 50 randomly chosen permutations, i. e., different orders of clouds in the superset 4.3, to make the results independent from the order of clouds.

We assume to reach the (statistical) truth for mean and standard deviation by analyzing all 33 clouds. Thus, Fig. 8 a shows that the virtual measurements approach true mean proportional to $1/\sqrt{N}$, where N is the number of analyzed clouds, as theoretical estimates suggest (e g., Chap. 5.4, Von Storch and Zwiers, 2001). However, the vertical velocity is by a factor of 1.8, and the LWC by a factor of 1.2 larger than the mean, which confirms the systematical deviation of one-dimensional measurements already explained for Fig. 6. By taking 15 examined clouds as a practicable number for real cloud measurements, Fig. 8 a shows that the mean properties of the vertical velocity deviate by ± 0.4 (20 %) and the LWC by ± 0.2 (15 %) from the (statistical) truth. Fig. 8 b shows that the standard deviation of virtual airplane measurements approaches a systematically lower value than the two-dimensional sets of data. This is a consequence of the larger sets of two-dimensional data which, accordingly, have a higher possibility to include more extreme values than the smaller sets of virtual airplane measurements. For 33 examined clouds, the standard deviations approach values of 0.9 and 0.6 for the vertical velocity and the LWC, respectively. By examining 15 clouds, these values deviate about ± 0.2 (20 %) and ± 0.1 (15 %) for the vertical velocity and the LWC, respectively. All in all, Fig. 8 shows, that quantities derived from 15 examined clouds have an uncertainty of about 20 %, which has to be taken into account for the interpretation of airplane measurements.

The helicopter pilots are in charge of the exact flight track and altitude during penetrating the cloud fields. Often it is difficult from the helicopter perspective to estimate the location of ACTOS with respect to the individual cloud to be sampled and only a real-time camera assists the people aboard. Therefore, it would be of interest to know how changes in height and horizontal location are influencing the statistics of typical cloud parameters such as vertical velocity w and liquid water mixing ratio q_l. To estimate the influence of slightly different flight paths on the sampling statistics four virtual measurement flights as described in Sec. 2.2 are performed in parallel but the flight paths are shifted by 20 m in both horizontal directions and to the vertical position (cf. Table 1). Fig. 9 shows w and q_l during a 10 km long flight track for all four flight paths. A single cloud penetration is enlarged to illustrate the differences encountered for the shifted flight paths. It is obvious that the mean structure of the cloud field is captured by all four paths and the PDF of both parameters are quite similar for the four data sets (see Fig. 10). The observed scatter for the four data sets $((x_{max} - x_{min})/\overline{x} \cdot 100\,\%)$ is 10 % for q_l and 20 % for w. This scatter – or sampling error–has to be considered in the interpretation of mean values and variances of airborne cloud observations.

5 Details of cloud edges from observations and LES

In this section the fine-scale structure of cloud edges as observed during CARRIBA is analyzed and compared with virtual flights in the BOMEX domain. Based on an analysis by Katzwinkel et al. (accepted) 40 actively growing clouds which are sampled in the period of April 13th and 14th 2011 were selected from the CARRIBA data set. In this context, 'actively growing clouds' are characterized by a mean updraft and a positive buoyancy in the cloud interior which itself is defined by a liquid

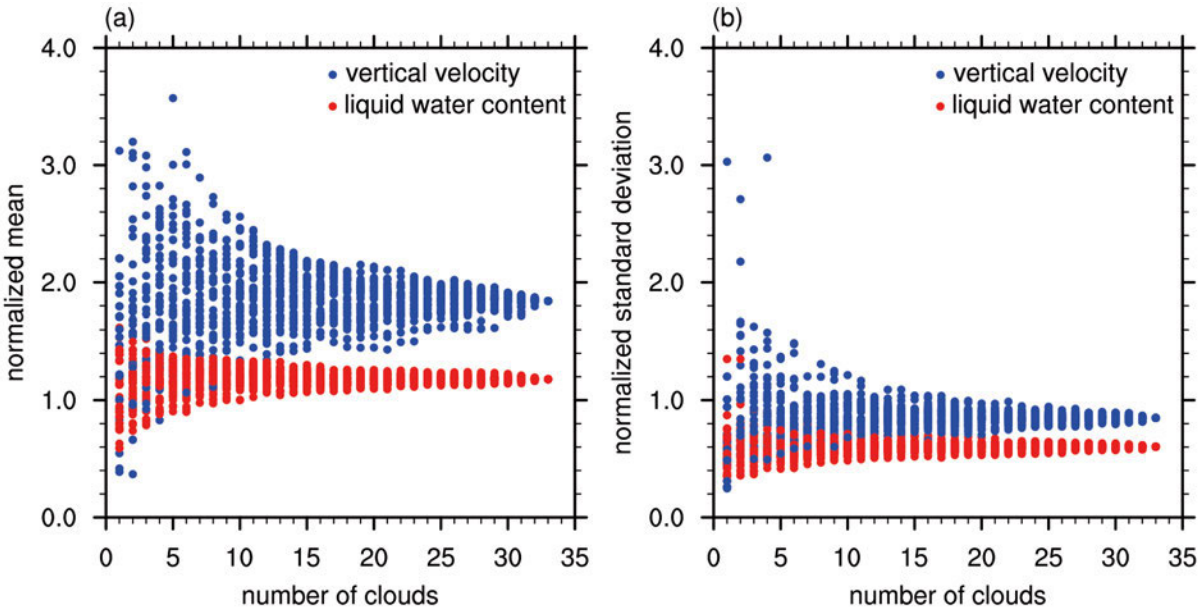

Figure 8: Normalized mean (a), and normalized standard deviation (b) as a function of the number of analyzed clouds for liquid water content (red circles) and vertical velocity (blue circles). 50 randomly chosen orders of 33 examined clouds are displayed. Values are normalized by the corresponding two-dimensional mean (see text for more details on the normalization).

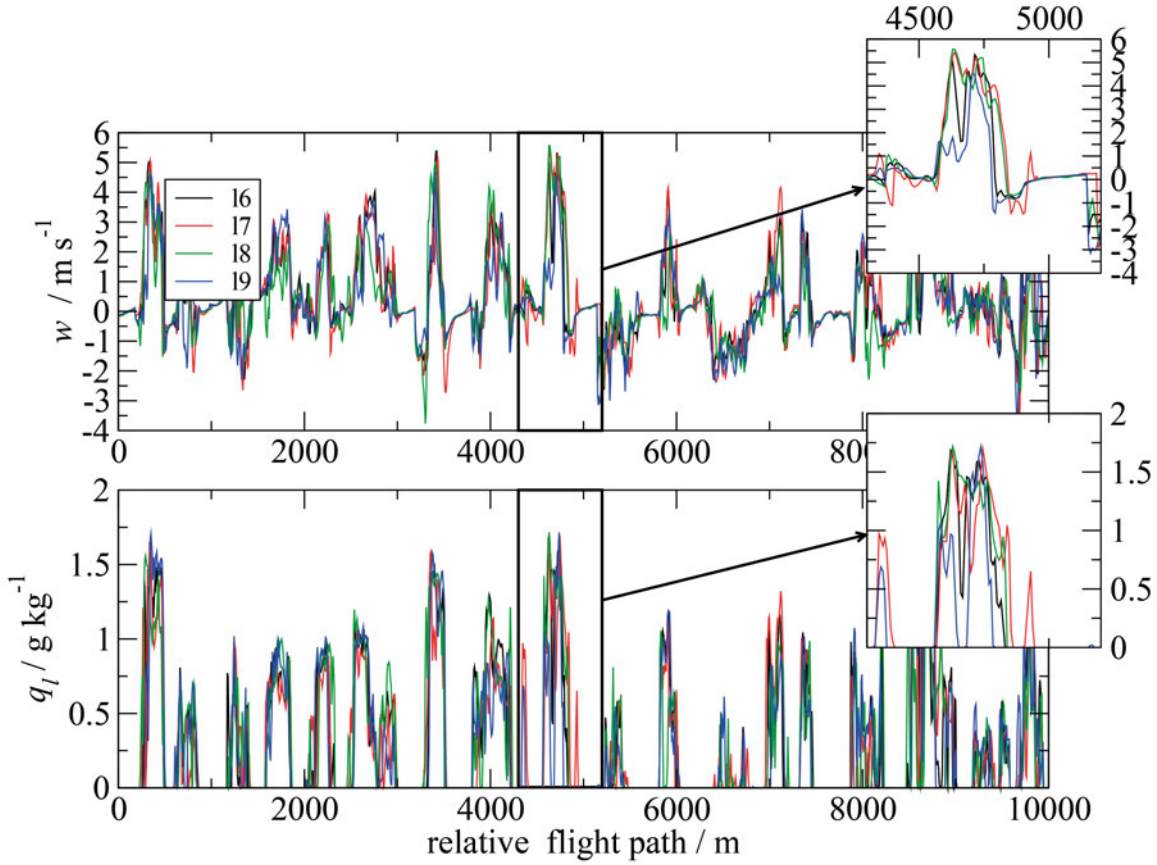

Figure 9: Vertical velocity in m s^{-1} (upper panel), and liquid water mixing ratio in g kg^{-1} (lower panel) as a function of relative flight path in m for four slightly shifted virtual flight paths (l6 to l9, see Table 1 for details) in the BOMEX-LES slightly below cloud top in around 1500 m. A short cloud penetration is shown as enlarged portion.

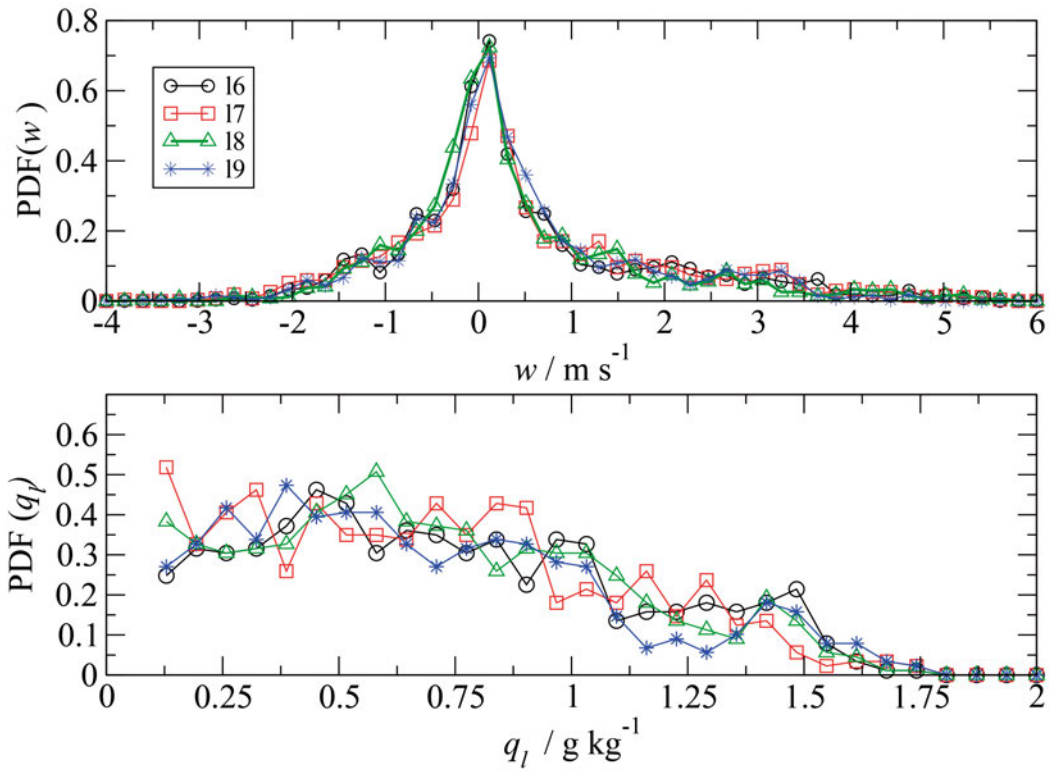

Figure 10: Probability density functions (PDF) of vertical velocity in $\mathrm{m\,s^{-1}}$ (upper panel), and liquid water content in $\mathrm{g\,kg^{-1}}$ (lower panel) for the same virtual flights shown in Fig. 9.

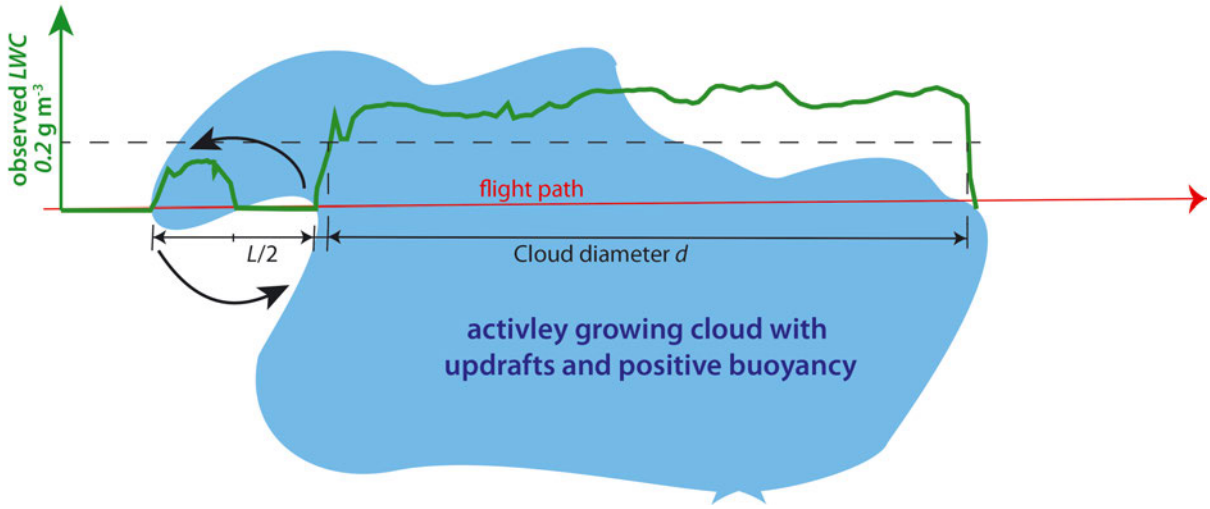

Figure 11: Schematic of an actively growing cumulus cloud (blue area) with the definition of cloud diameter d and a typical entraining eddy of size L at the left cloud edge. A typical flight path (red line) illustrates an airborne penetration of the cloud including the observed LWC (green line). The sketch is not in scale.

Table 1: Overview of four virtual flights l6 to l9 in the BOMEX domain with slightly shifted flight path.

flight	$\overline{q_l}$ / g kg^{-1}	σ_{q_l}	$\overline{w}$ / m s^{-1}	σ_w	Comment
l6	0.29	0.43	0.39	1.37	reference flight 100 below cloud top
l7	0.28	0.41	0.42	1.45	as l6 but 20 m lower
l8	0.29	0.41	0.31	1.33	as l6 but +20 m horizontally shifted
l9	0.26	0.41	0.32	1.26	as l6 but −20 m horizontally shifted

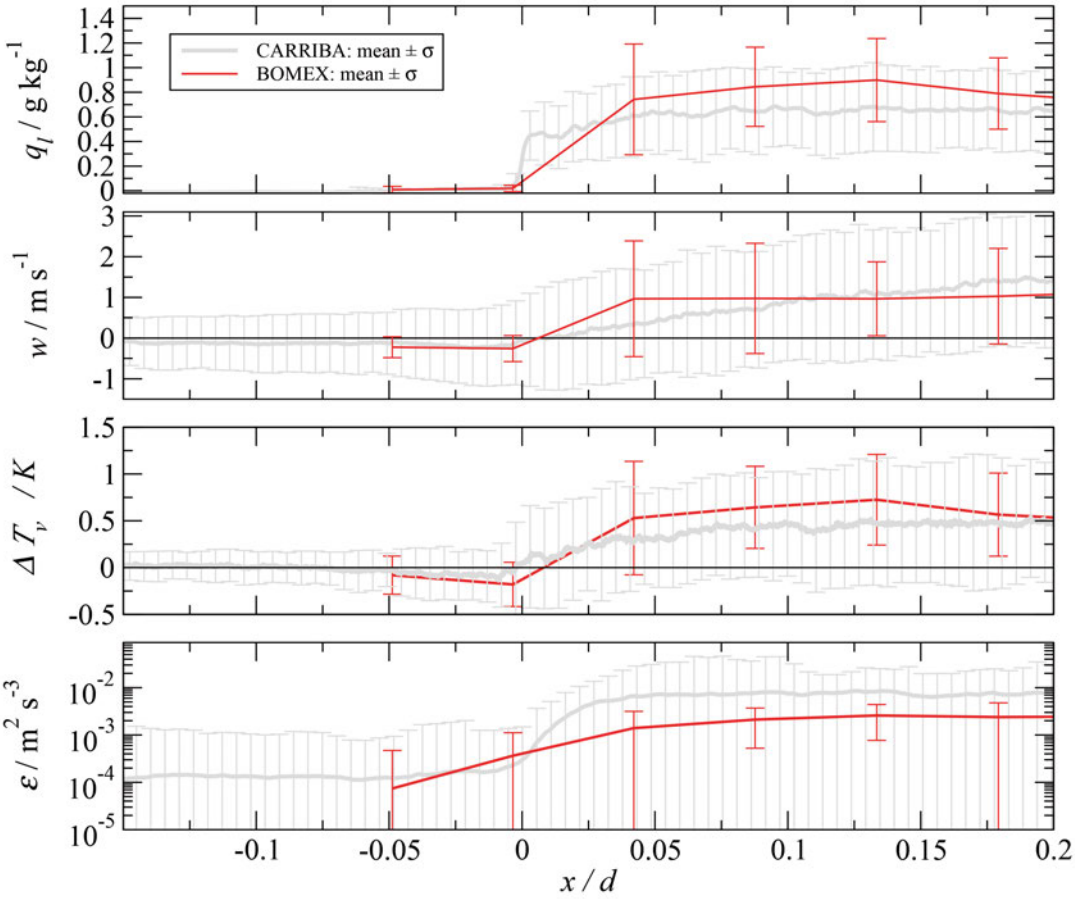

Figure 12: Average liquid water mixing ratio in g kg^{-1}, vertical velocity in m s^{-1}, the difference of virtual temperature between cloud-free environment and cloud interior in K, and the local energy dissipation rate in m^{2}s^{-3} (from top to bottom) as a function of distance to cloud edge normalized by the cloud diameter d for CARRIBA observations (40 analyzed clouds, gray line) and BOMEX-LES (15 analyzed clouds, red line). The cloud edge is located at $x/d = 0$, positive values of the abscissa are located inside the cloud. Error bars denote a 1-σ bandwidth.

water content LWC $\geq 0.2\,\mathrm{g\,m^{-3}}$. For the averaging over individual clouds, the flight path x is normalized by the diameter d of the cloud interior and $x/d = 0$ is set at cloud edge and the averaging has been performed over bins with a width of $\Delta x/d = 0.05$. Fig. 11 shows a schematic of a cloud including the definitions of the typical cloud dimensions.

Fig. 12 shows selected parameters ($q_l, w, \Delta T_\mathrm{v}$, and ε) as a function of x/d. Here, ΔT_v is the difference of the virtual temperature T_v between the cloud-free environment and the cloud. Therefore, we can identify this difference as a measure of the buoyancy in the cloud. The virtual temperature $T_\mathrm{v} \approx c^2/(\gamma R)$ is calculated from the speed of sound c which is measured by an ultrasonic anemometer/thermometer. Here, $\gamma = 1.4$ is the adiabatic coefficient and $R = 287\,\mathrm{J\,kg^{-1}\,K^{-1}}$ is the gas constant of dry air. A discussion about using such a device under cloudy conditions can be found in Cruette et al. (2000).

The averaged CARRIBA cloud data show a sharp increase of q_l at cloud edge from zero to about 60 to 80 % of the mean cloud interior value. The mean taken over BOMEX clouds exhibits a somewhat smoother cloud edge in terms of q_l (cf. Fig. 12). The reason for this behavior is obviously the lower resolution of the LES. Assuming a typical cloud diameter of $d \approx 100$ m or so, $x/d = 0.05$ results in the grid space of the LES (5 m). However, the large variance of q_l at the cloud edge

indicates that the lateral entrainment of cloud-free air is visible in LES too. The general structure of the mean cloud edge and the bandwidth agree thus qualitatively.

The mean structure of w and ΔT_v is also quite similar; in the cloud-free environment both parameters show a comparably small variability with $\sigma_w \approx 0.5\,\mathrm{m\,s^{-1}}$ and $\sigma_{T_v} \approx 0.25\,\mathrm{K}$ around zero increasing towards the cloud interior with values of $\sigma_w \approx 1.5\,\mathrm{m\,s^{-1}}$ and $\sigma_{T_v} \approx 0.6\,\mathrm{K}$. One interesting feature are the small local minima in w and T_v around cloud edge for $-0.05 \leq x/d \leq +0.05$. These minima are most obvious for the negative 1-σ bars and are a clear indication for frequently observed subsiding shells around cumulus clouds. Such shells have been observed, both in LES (Heus and Jonker, 2008) and the CARRIBA data (Katzwinkel et al., accepted). The main reason for these downdrafts are negatively buoyant air parcels which are caused by evaporative cooling of cloud droplets at the cloud edge as a consequence of entrainment. Because the flight path has been scaled with the cloud diameter d and since there is no evidence that the width of the subsiding shell scales in the same way, averaging partly smears out the structure of the subsiding shells in Fig. 12. A more detailed discussion of subsiding shells can be found in Heus and Jonker (2008) and Katzwinkel et al. (accepted).

The local energy dissipation rate (here 'local' means a spatial resolution of about 20 m, see Sec. 2.4 for more details) shows on average mean values of $\varepsilon \sim 10^{-4}\,\mathrm{m^2\,s^{-3}}$ for the cloud-free environment. Around cloud edge, ε increases by one or two orders of magnitude and frequently a small local maximum can be found at cloud edge. In the averaged plot this is only visible for the positive $1-\sigma$ error bar of ε for $0 < x/d < 0.1$ but the maximum is well pronounced for two selected cloud penetrations for CARRIBA and BOMEX data in Fig. 13. These local maxima are caused by strong vertical shear in the region where the downdrafts of the subsiding shell are close to the updrafts in the cloud core regions (Siebert et al., 2006c).

Both the structure of the subsiding shell and the corresponding increase of the turbulence level are now illustrated in one example for a CARRIBA and BOMEX cloud edge. Fig. 13 shows two cloud penetrations through actively growing cumulus clouds. Note that in this plot the x-axis is the absolute flight path. For the two selected clouds, the subsiding shell is much more pronounced compared to the averaged CARRIBA observations. We can observe now a very similar structure for ΔT_v. Both quantities, w and ΔT_v, drop off at $x \approx 5$ m which is the same location where q_l indicates a small amount of liquid water. This corroborates the idea of an evaporating cloud area which results in the negative buoyancy and, consequently in an downdraft. Note that for the CARRIBA example the width of this subsiding area is only about 10 m.

Individual clouds are often characterized by one or more local minima around the cloud edges where q_l drops off to almost zero. This phenomenon is illustrated in the enlarged portion of Fig. 13 where q_l indicates a 2 to 3 m cloud-free flight path. One plausible explanation for this structure in q_l is that these minima can be caused by entraining eddies and the horizontal dimension of these structures gives an indication for the scale L of the largest entraining eddies at cloud edge. This picture of the eddy-like structure of the cloud edge is illustrated at the left cloud side in Fig. 11. The red line in Fig. 11 indicates a possible airborne penetration and the green line shows the corresponding LWC observation with the 'cloud hole' of length $L/2$ caused by the eddy.

6 Subgrid scale turbulence study by direct numerical simulations

Although the BOMEX simulation have been run at a rather fine grid already, we have seen in the last section that they can give us a qualitatively correct picture of the cloud edge only. The finest grid resolution in the LES is a few meters which is still three to four orders of magnitude above the Kolmogorov length η_K. In addition, we identified the width of the subsiding shell with about 10 m, inaccessible to a DNS. With a grid resolution as fine as 1 mm we are able only to study volumes of size $V \leq (2\,\mathrm{m})^3$.

The important question that comes to mind is therefore, how much information gets lost in a subgrid scale model and how important is this information? It is well-known that particularly the smaller scales obey the highest spatial intermittency. The last part of our manuscript will make a first step into this direction. Therefore we conducted a series of four DNS runs which apply the pseudospectral method in a cubic box of side length L_{DNS} with cyclic boundary conditions. The variables determining the runs are listed in Table 2 together with essential statistical quantities which characterize the fluid turbulence. The range of obtained Taylor microscale Reynolds number varies between 89 and 252. This quantity is defined as

$$R_\lambda = \sqrt{\frac{5}{3\nu\varepsilon}}\, u_{\mathrm{rms}}^2\,, \tag{6.1}$$

with the kinematic viscosity ν, the mean kinetic energy dissipation rate ε. The turbulence is sustained in a statistically stationary regime by an additional volume driving term which is added to the right hand side of the Navier-Stokes equations and which contains a fixed large-scale energy injection rate $\dot{E}_{\mathrm{in}}$ as a parameter (see Schumacher et al., 2007, for more details). For a stationary turbulent cascade, the mean energy dissipation rate is fixed to $\varepsilon = \dot{E}_{\mathrm{in}}$. Consequently the Kolmogorov length η_K is determined as well. It allows us thus also to prescribe dissipation to a value which is found at the smallest grid size of the LES. As already mentioned at the beginning, we will limit our studies to the pure hydrodynamic case. The typical variability as well as the mean of the (surrogate) energy dissipation rate, both of which are determined in the LES at the smallest grid

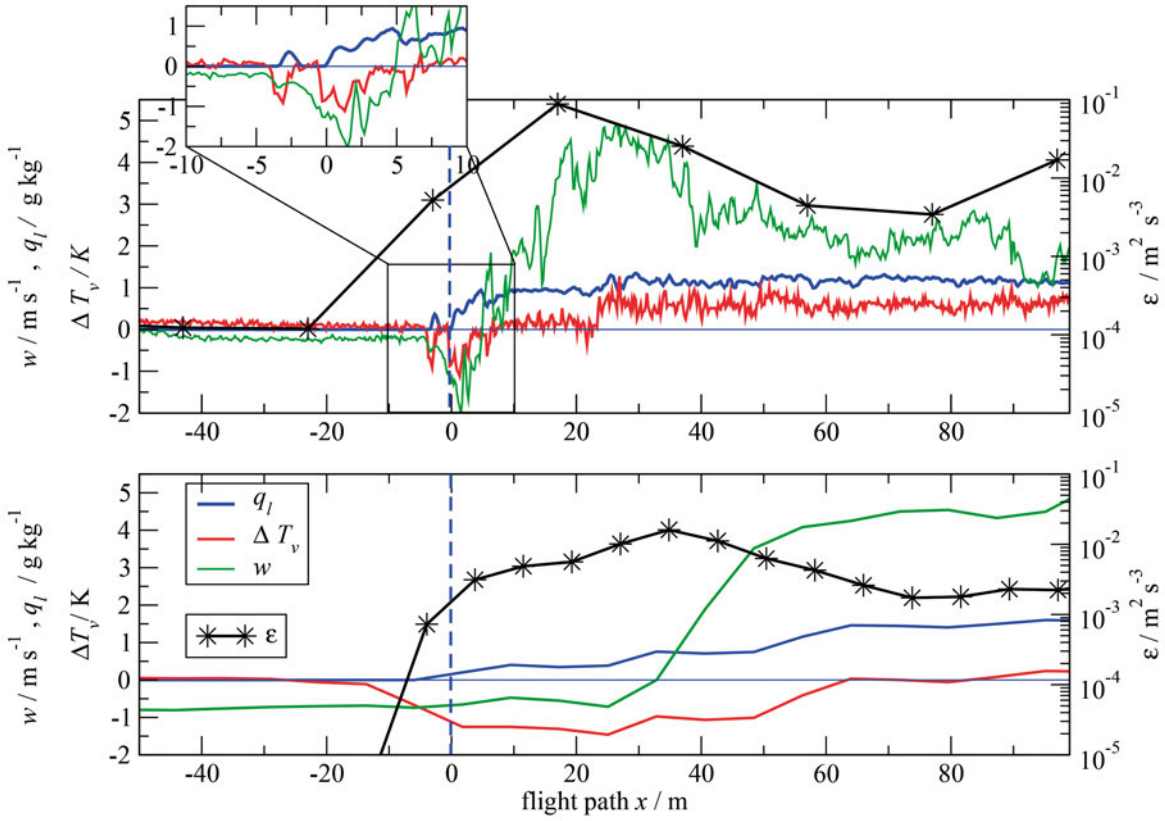

Figure 13: Liquid water mixing ratio in g kg^{-1} (blue line), the difference of virtual temperature between cloud-free environment and cloud interior in K (red line), vertical velocity in m s^{-1} (green line), and the local energy dissipation rate in m^{2}s^{-3} (black line) as a function of absolute flight path as a distance from cloud edge in m for a single observed CARRIBA cloud (upper panel) and a single simulated BOMEX cloud (lower panel). The cloud edge is located at $x = 0$ m, positive values of the abscissa are located inside the cloud.

Table 2: Parameters of the four DNS runs. We list the side length of the cubic volume L_{DNS}, the (equidistant) grid spacing a, the number of grid points in each space direction, N, the Kolmogorov length $\eta_K = \nu^{3/4}/\varepsilon^{1/4}$, the mean kinetic energy dissipation rate ε, the root mean square velocity $u_{\mathrm{rms}} = \langle u^2 + v^2 + w^2 \rangle^{1/2}$, the large-scale eddy turnover time $T_L = L_{\mathrm{DNS}}/u_{\mathrm{rms}}$. Finally we give the Taylor microscale Reynolds number R_λ which is defined in equation (6.1) and the large-scale Reynolds number $Re = u_{\mathrm{rms}} L_{\mathrm{DNS}}/\nu$. The kinematic viscosity of air is $\nu = 0.15\,\mathrm{cm^2 s^{-1}}$.

Case	L_{DNS} / m	a / mm	N	η_K / mm	ε / cm^2 s^{-3}	u_{rms} / cm s^{-1}	T_L / s	R_λ	Re
1	0.512	1	512	1.0	33.75	12.5	4.1	89	4267
2	1.024	2	512	1.0	33.75	16.0	6.4	147	10923
3	2.048	2	1024	1.0	33.75	20.7	9.9	252	28262
4	1.024	2	512	0.8	67.50	20.2	5.1	166	13790

size, are shown in Fig. 14 as a function of height. We display data inside and outside of clouds of the BOMEX case described in Sec. 2.2. Dissipation is significantly enhanced inside the cloud compared to its environment. It can be also seen that the ε-values we use in the DNS are well inside the range obtained in the LES at the cloud boundary.

The situation is slightly different for the velocity data. Fig. 15 shows the mean vertical velocity component in- and outside the cloud together with the standard deviation about the mean (in gray). In order to compare these magnitudes with our DNS results, we will relate the root-mean-square values of the velocity to the data in Fig. 15. Note that we have no mean flow and equally large velocity fluctuations in all three space directions in the DNS. The amplitudes which we report in Table 2 are smaller. Cases 1, 2 and 3 allow us to extrapolate the velocity fluctuations by assuming a power law that fits to the three data points. In detail, we obtained $u_{\mathrm{rms}} = U_0 (L_{\mathrm{DNS}}/L_0)^\beta$ with $U_0 = 0.16\,\mathrm{m\,s^{-1}}$ and $\beta = 0.37$. $L_0 = 1\,\mathrm{m}$ is a reference length to bring the law into a dimensionally correct form. This would result

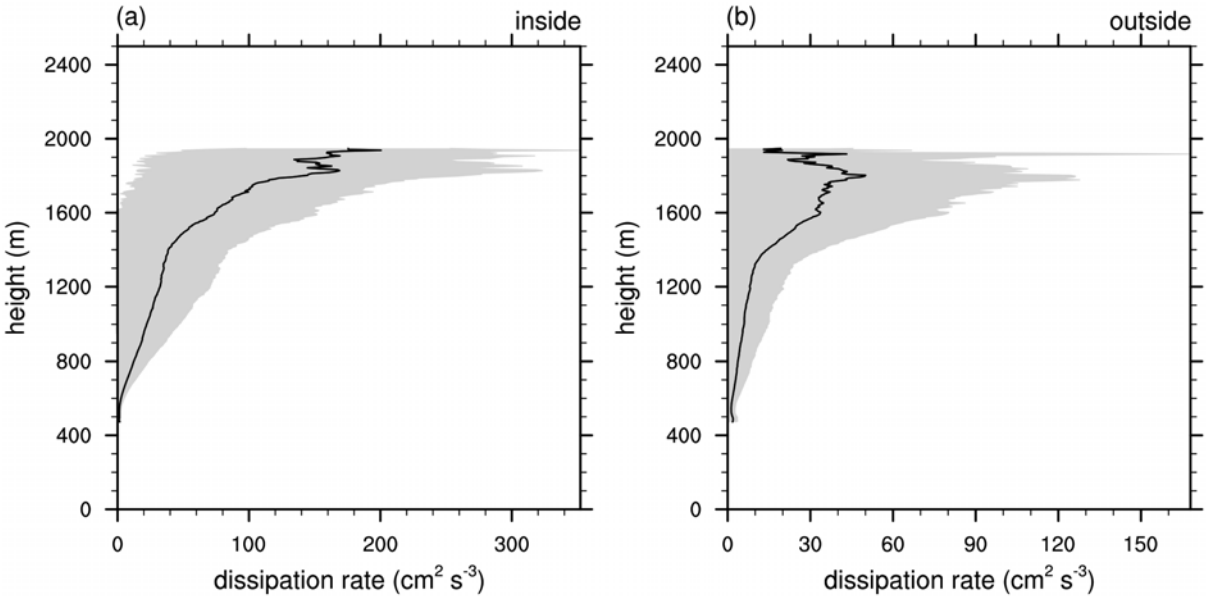

Figure 14: Averaged BOMEX-LES profiles of local energy dissipation rate in $\mathrm{cm^2 s^{-3}}$ as a function of height in m for grid points located 5 m inside the cloud (a), and 5 m outside the cloud (b). Shaded area around the continuous line has a width of two standard deviations. Note that different scales are used on the abscissa.

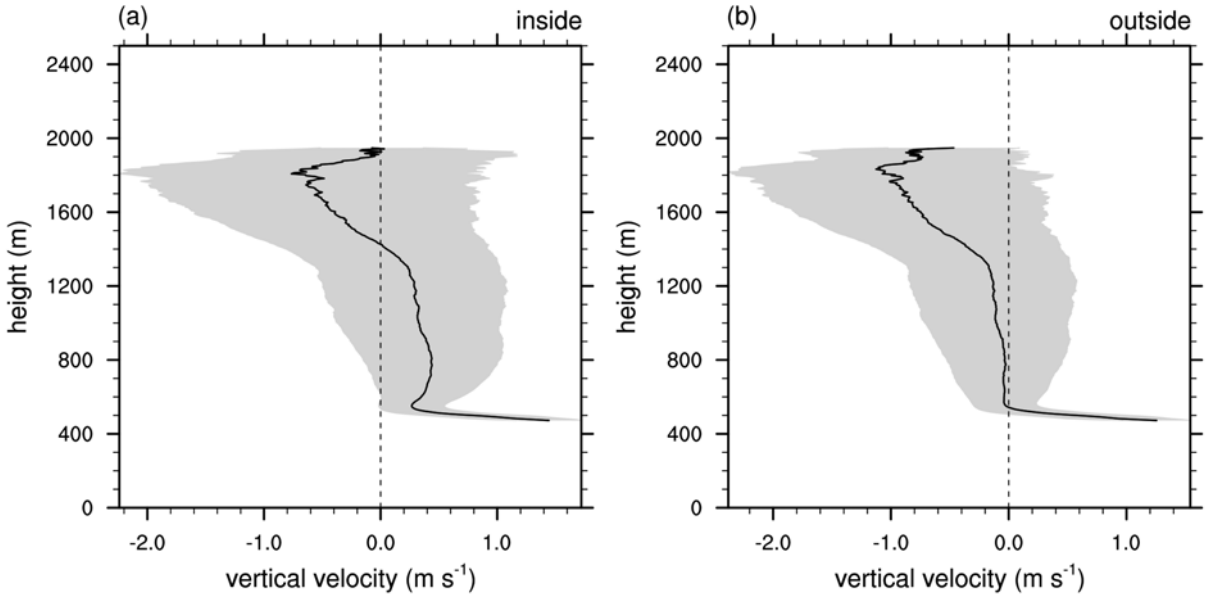

Figure 15: As Fig. 14, but for averaged BOMEX-LES profiles of vertical velocity in $\mathrm{m\,s^{-1}}$. The short dashed line marks zero velocity.

in a value of $u_{\mathrm{rms}} \approx 40\,\mathrm{cm\,s^{-1}}$ for a box size of about 10 meters and of $u_{\mathrm{rms}} \approx 70\,\mathrm{cm\,s^{-1}}$ for 50 meters. These values are a coarse estimate only since the DNS are for isotropic turbulence and satisfy $w_{\mathrm{rms}} = 1/3\,u_{\mathrm{rms}}$. For the turbulence in the cloud one can expect that the vertical fluctuations are larger than the horizontal ones due to evaporative cooling as discussed by Malinowski et al. (2008). The series was in addition obtained for a small mean dissipation rate. Table 2 shows also that a stronger driving of the box turbulence enhances ε and consistently the velocity fluctuations significantly (see cases 2 and 4 at the same box size). Both runs are thought to reflect the situation as illustrated in Fig. 16. The finest resolution of the LES grid was 5 meters and the turbulent fine structure has been tracked in three neighboring mesh cells positioned at the edge of the cloud. The LES data show consistently that the kinetic energy dissipation has higher amplitudes in the interior compared to the vicinity of the cloud.

We can expect that a coarser computational grid will smooth out the high-amplitude events of the energy dissipation rate. This has been seen already in the last section where LES data have been compared with higher-resolution observations. To reformulate our question from above: which impact does the coarser resolution have on the velocity field statistics? We there-

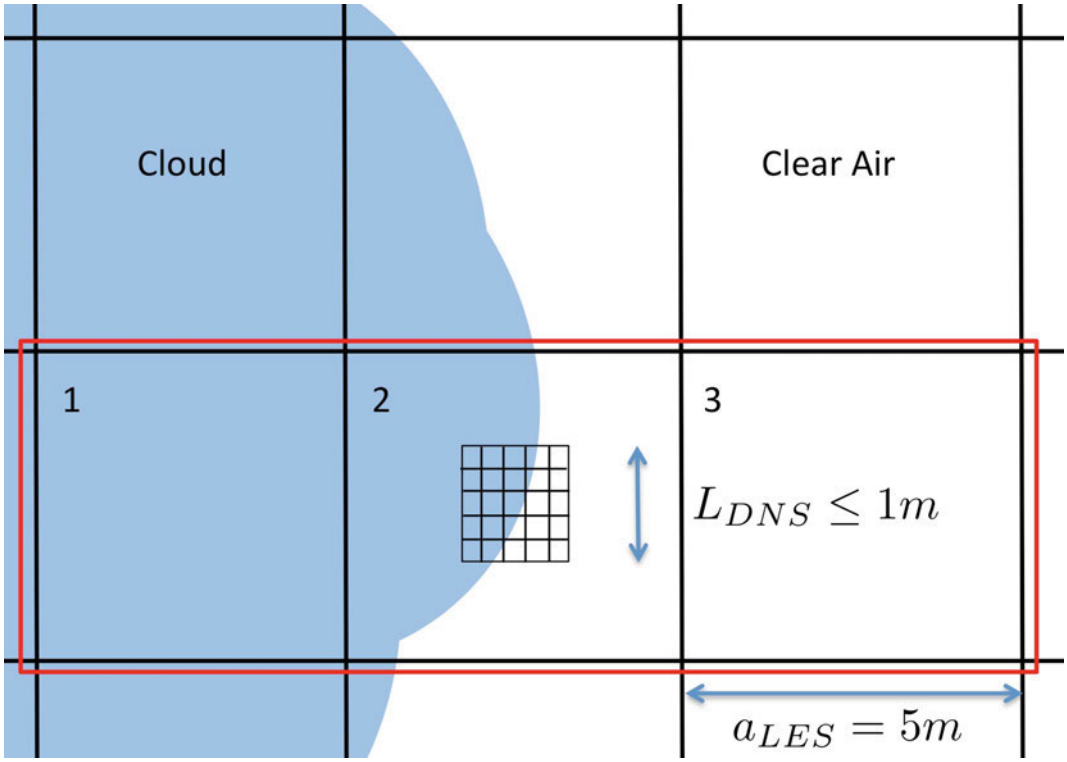

Figure 16: The sketch illustrates the different resolutions as present in the LES and the DNS. The investigations on the matching of both methods focus to three LES grid cells which are co-moving with the evolving edge of a cloud. Grid cell 1 is completely inside the cloud, grid cell 2 is at the edge and grid cell 3 outside the cloud.

fore collect statistics for which high dissipation rate amplitudes are excluded, or in other words, we incorporate velocity data at grid sites only at which the energy dissipation does not exceed a threshold. For the DNS with the biggest simulation domain, case 3, we applied the following procedure which is shown in Fig. 17. We display the PDF of the longitudinal velocity increment (the second moment of this PDF results in the well-known second-order structure function when evaluated for varying r) taken over two different distances, one in the viscous range, at $r \approx 2\eta_K$, and the other at the small-scale end of the inertial subrange, at $r \approx 40\eta_K$. It is well-known that with decreasing separation r the intermittency increases as manifest in the fatter tails of the PDF (see, e. g., Frisch, 1995). The coarsening is mimicked by conditioning the velocity increments to the amplitude of the dissipation rate at the increment points. When the threshold is successively decreased, one detects a clear suppression of the intermittency. The smaller the scale separation the stronger is this effect. Similar observations have been reported by Kholmyansky and Tsinober (2009) for measurements in an atmospheric boundary layer. This analysis demonstrates clearly that intermittent turbulent fluctuations will be significantly suppressed, in particular at the very small scales. In other words, coarse-graining drives the turbulence statistics towards the Gaussian case and diminishes the intermittent fluctuations and thus the fat tails of the distributions. Thus it can be expected that LES will always display a reduced level of small-scale intermittency. This circumstance is not incorporated in standard subgrid parametrizations which model a continuation of a classical Kolmogorov cascade towards the small scales. Our analysis does however also show that such an effective filtering becomes increasingly insensitive when the scale separation (or in other words, the resolved scale) becomes larger. A next step would be to study how such a effective filtering affects the microphysical properties of the cloud droplets at the cloud edge.

7 Summary and discussion

The multi-scale process of cumulus convection with a focus on entrainment and mixing was examined by a combination of airborne observations, large-eddy simulations (LES), and direct numerical simulations (DNS), which were essentially needed to cover all relevant scales. Moreover, this multi-method approach was used to review their individual results and to identify their shortcomings. With a focus on the trade-wind region and its ubiquitous shallow cumuli, three flights carried out with the helicopter-borne observation system ACTOS during the CARRIBA campaign were found to compare well with the established BOMEX LES-case, which has been chosen to drive our LES for this study. The profiles of potential temperature and specific humidity of CARRIBA and BOMEX compare well although CARRIBA was about 1 K warmer and the trade inversion was

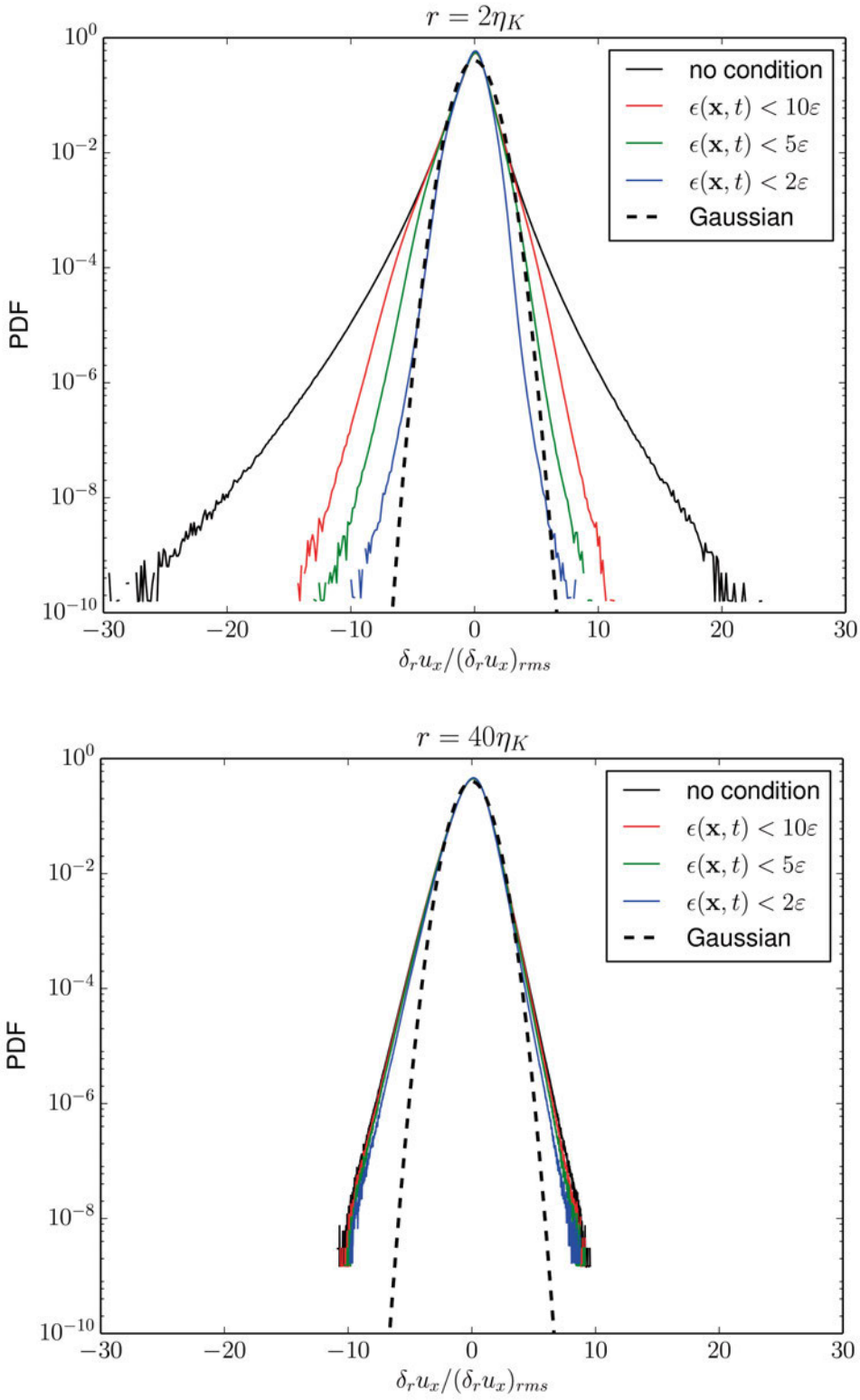

Figure 17: Probability density functions (PDF) of the longitudinal velocity increments. The increments are taken over different distances r in the top and bottom figures as indicated in the title. Additionally they are either unconditioned or conditioned to low dissipation events as indicated in the legend.

less pronounced during CARRIBA. However, the latter is not problematic since our observations were bounded to the cloud-layer, i. e., below the inversion.

The estimation of the local energy dissipation rate by the second-order structure function as used for real ACTOS flights was applied to the data gained from virtual flights in the BOMEX domain. These dissipation rates compare well to the dissipation rate estimated by the LES subgrid model.

Since the entrainment and subsequent mixing of cloud-free and cloudy air is associated with the evaporation of cloud droplets and hence evaporative cooling, entrainment and mixing are visible as fluctuations of liquid water mixing ratio and temperature, which we used to study mixing in the BOMEX and CARRIBA data. For both sets, we found quantitative agreement of the linear relationship between fluctuations of liquid water mixing ratio and temperature. However, the fluctuations are lower than expected from purely adiabatic processes. Thus, this deviation is a measure of diabatic processes as the mixing at the clouds lateral edge and shows that LES reproduces these processes in a good quantitative agreement with observational data.

In order to validate the measurements of ACTOS, we compared the virtual (one-dimensional) airborne measurements to the corresponding two-dimensional cross-section of the cloud at the virtual height of the measurement. This comparison showed that one-dimensional measurements overestimate the mean values of liquid water content and vertical velocity by factors of 1.2 and 1.8, respectively, and underestimate their standard deviation by factors of 0.6 and 0.9, respectively. By discussing simple geometrical arguments, we also showed that one-dimensional measurements overestimate the cloud core and its higher values of liquid water content and vertical velocity. The systematically smaller values of the standard deviation might result from the smaller statistical basis of the one-dimensional measurements. We also quantified the sampling error of airborne measurements resulting from slight displacements of the flight track by comparing four different tracks each displaced by 20 m to the left, to the right, and down in an identical simulation, i. e., all four flight penetrated the same cloud. Such displacements need to be taken in account for any real airborne measurement and result in an sampling error of 10 % for the liquid water content and 20 % for the vertical velocity.

Since the cloud edge is the location of entrainment and subsequent mixing, we examined the ability of our BOMEX simulations to resolve the fine structure of this important part of the cloud. Average cloud edges of BOMEX LES and CARRIBA observations agree qualitatively although the edge of BOMEX is smoother due to the relatively coarse grid spacing of 5 m. Note however, that this grid resolution is not exceptionally coarse for LES studies. The cloud-clear air interface is resolved here by two or three grid cells. The CARRIBA data can unravel many details of the interface, in particular the structure of a subsiding shell with a strong jump in virtual temperature, vertical velocity and LWC. This is in line with a significant local enhancement of the energy dissipation. It can thus be expected that the main contribution originates from the strong horizontal shear of the vertical velocity which as been discussed in Siebert et al. (2006c). The present studies suggest even to compare the observation with DNS in this respect which should be able soon to simulate a distance of 1 to 3 m. It would tell us if the subsiding shell is locally generated or requires the convective cloud with its large-scale circulation as a whole. Efforts in this direction are under way. In the last section of our study we suggested a quantitive way to measure the impact of the coarse LES grid resolution on the velocity statistics. The present result can be summarized compactly as follows: Coarse-graining drives the turbulence statistics to Gaussian values and removes intermittency. The next step has to be an incorporation of the cloud droplet dynamics in order to see how the coarse grids affect the individual droplets (or super droplets, e. g., used by Riechelmann et al., 2012) and how their collective dynamics feeds back on the larger-scale turbulence structure. Our present work demonstrated clearly that a joint methods approach is a promising path to unravel the open problems with respect to entrainment processes. Significant efforts are however still necessary to obtain a better overlap in the ranges of scales which can be covered by the different methods.

Acknowledgments

The authors thank for financial support by the priority program SPP 1276 Metström by the Deutsche Forschungsgemeinschaft (grants RA 617/25-2, SI 1534/2, SCHU 1410/9). JS wishes to thank for additional support by the European COST Action MP806 Particles in turbulence and Grant No. 1072-6.14/2009 of the German-Israeli Foundation. We thank two anonymous reviewers for their constructive comments. The LES-simulations have been carried out on the SGI-ICE systems of the North-German Supercomputing Alliance (HLRN). The DNS have been carried out on the JUROPA cluster at the Jülich Supercomputing Centre with grant HIL08. Part of the CARRIBA project was funded by the Deutsche Forschungsgemeinschaft grant SI 1534/3.

References

Abma, D., T. Heus, J.P. Mellado, 2013: Direct numerical simulation of evaporative cooling at the lateral boundary of shallow cumulus clouds. – J. Atmos. Sci. **70**, 2088–2102.

Albrecht, B.A., C.S. Bretherton, D. Johnson, W.H. Scubert, A. S. Frisch, 1995: The atlantic stratocumulus transition experiment – ASTEX. – Bull. Am. Meteor. Soc. **76**, 889–904.

Clyne, J., P. Mininni, A. Norton, M. Rast, 2007: Interactive desktop analysis of high resolution simulations: application to turbulent plume dynamics and current sheet formation. – New J. Phys. **9**, 301.

Cruette, D., A. Marillier, J. Dufresne, J. Grandpeix, P. Nacass, H. Bellec, 2000: Fast temperature and true airspeed measurements with the airborne ultrasonic anemometer–thermometer (ausat). – J. Atmos. Oceanic Technol. **17**, 1020–1039.

Cuijpers, J., P. Duynkerke, 1993: Large eddy simulation of trade wind cumulus clouds. – J. Atmos. Sci. **50**, 3894–3908.

Davidson, B., 1968: The Barbados oceanographic and meteorological experiment. – Bull. Am. Meteor. Soc. **49**, 928–934.

de Roode, S.R., A. Los, 2008: The effect of temperature and humidity fluctuations on the liquid water path of non-precipitating closed-cell stratocumulus clouds. – Quart. J. Roy. Meteor. Soc. **134**, 403–416.

Deardorff, J.W., 1976: Usefulness of liquid-water potential temperature in a shallow-cloud model. – J. Appl. Meteorol. **15**, 98–102.

Deardorff, J.W., 1980: Stratocumulus-capped mixed layers derived from a three-dimensional model. – Bound.-Layer Meteor. **18**, 495–527.

Frisch, U., 1995: Turbulence: The legacy of A. N. Kolmogorov. – Cambridge University Press, Cambridge, 289.

Gerber, H., B.G. Arends, A.S. Ackerman, 1994: New microphysics sensor for aircraft use. – Atmos. Res. **31**, 235–252.

Gerber, H.E., G.M. Frick, J.B. Jensen, J.G. Hudson, 2008: Entrainment, mixing and microphysics in trade-wind cumulus. – J. Meteorol. Soc. Japan **86A**, 89–106.

Grabowski, W.W., 1989: Numerical experiments on the dynamics of the cloud-environment interface: Small cumulus in a shear-free environment. – J. Atmos. Sci. **46**, 3513–3541.

Haman, K., S.P. Malinowski, 1996: Temperature measurements in clouds on a centimeter scale - Preliminary results. – Atmos. Res. **41**, 161–175.

Heus, T., H.J.J. Jonker, 2008: Subsiding shells around shallow cumulus clouds. – J. Atmos. Sci. **65**, 1003–1018.

Heus, T., C.F. J. Pols, H.J. J. Jonker, H.E.A. Van den Akker, D.H. Lenschow, 2009: Observational validation of the compensating mass flux through the shell around cumulus clouds. – Quart. J. Roy. Meteor. Soc. **135**, 101–112.

Holland, J.Z., E.M. Rasmusson, 1973: Measurements of the atmospheric mass, energy, and momentum budget over a 500-kilometer square of tropical ocean. – Mon. Wea. Rev. **101**, 44–55.

Katzwinkel, J., H. Siebert, T. Heus, R.A. Shaw, accepted: Measurements of turbulent mixing and subsiding shells in trade wind cumuli. – J. Atmos. Sci.

Kholmyansky, M., A. Tsinober, 2009: On an alternative explanation of anomalous scaling and how well-defined is the concept of inertial range. – Phys. Lett. A **373**, 2364–2367.

Kumar, B., F. Janetzko, J. Schumacher, R.A. Shaw, 2012: Extreme responses of a coupled scalar-particle system during turbulent mixing. – New J. Phys. **14**, 115020.

Kumar, B., J. Schumacher, R.A. Shaw, 2013: Cloud microphysical effects of turbulent mixing and entrainment. – Theor. Comput. Fluid Dynam. **27**, 361–376.

Kumar, B., J. Schumacher, R.A. Shaw, 2014: Lagrangian mixing dynamics at the edge of a cloud. – J. Atmos. Sci. **71** 2564–2580.

Malinowski, S.P., M. Andrejczuk, W.W. Grabowski, P. Korczyk, T.A. Kowalewski, P.K. Smolarkiewicz, 2008: Laboratory and modeling studies of cloud-clear air interfacial mixing: anisotropy of small-scale turbulence due to evaporative cooling. – New J. Phys. **10**, 075020.

Malkus, J.S., 1954: Some results of a trade-cumulus cloud investigation. – J. Meteorol. **11**, 220–237.

Malkus, J.S., 1956: On the maintenance of the trade winds. – Tellus **8**, 335–350.

Malkus, J.S., 1958: On the structure of the trade wind moist layer. – Pap. Phys. Oceanogr. Meteor. **13**, 1–47.

Matheou, G., D. Chung, L. Nuijens, B. Stevens, J. Teixeira, 2011: On the fidelity of large-eddy simulation of shallow precipitating cumulus convection. – Mon. Wea. Rev. **139**, 2918–2939.

Raasch, S., T. Franke, 2011: Structure and formation of dust devil–like vortices in the atmospheric boundary layer: A high-resolution numerical study. – J. Geophys. Res. **116**(D16), published online.

Raasch, S., M. Schröter, 2001: PALM - A large-eddy simulation model performing on massively parallel computers. – Meteorol. Z. **10**, 363–382.

Riechelmann, T., Y. Noh, S. Raasch, 2012: A new method for large-eddy simulations of clouds with lagrangian droplets including the effects of turbulent collision. – New J. Phys. **14**, 065008.

Schröter, M., J. Bange, S. Raasch, 2000: Simulated airborne flux measurements in a LES generated convective boundary layer. – Bound-Layer Meteor. **95**, 437–456.

Schumacher, J., K.R. Sreenivasan, V. Yakhot, 2007: Asymptotic exponents from low-reynolds-number flows. – New J. Phys. **9**, 89, DOI:10.1088/1367-2630/9/4/089.

Siebert, H., A. Muschinski, 2001: Relevance of a tuning-fork effect for temperature measurements with the Gill Solent HS ultrasonic anemometer-thermometer. – J. Atmos. Ocean. Technol. **18**, 1367–1376.

Siebert, H., K. Lehmann, M. Wendisch, 2006a: Observations of small scale turbulence and energy dissipation rates in the cloudy boundary layer. – J. Atmos. Sci. **63**, 1451–1466.

Siebert, H., H. Franke, K. Lehmann, R. Maser, E.W. Saw, D. Schell, R.A. Shaw, M. Wendisch, 2006b: Probing fine-scale dynamics and microphysics of clouds with helicopter-borne measurements. – Bull. Am. Meteor. Soc. **87**, 1727–1738.

Siebert, H., K. Lehmann, M. Wendisch, R. Shaw, 2006c: Small-scale turbulence in clouds. – In: 12th Conference on Cloud Physics, 10–14 July, Madison, WI, USA.

Siebert, H., M. Beals, J. Bethke, E. Bierwirth, T. Conrath, K. Dieckmann, F. Ditas, A. Ehrlich, D. Farrell, S. Hartmann, M.A. Izaguirre, J. Katzwinkel, L. Nuijens, G. Roberts, M. Schäfer, R.A. Shaw, T. Schmeissner, I. Serikov, B. Stevens, F. Stratmann, B. Wehner, M. Wendisch, F. Werner, H. Wex, 2013: The fine-scale structure of the trade wind cumuli over Barbados – an introduction to the CARRIBA project. – Atmos. Chem. Phys. **13**, 10061–10077.

Siebesma, A.P., C.S. Bretherton, A. Brown, A. Chlond, J. Cuxart, P.G. Duynkerke, H. Jiang, M. Khairoutdinov, D. Lewellen, C.-H. Moeng, E. Sanchez, B. Stevens, D. Stevens, 2003: A large eddy simulation intercomparison study of shallow cumulus convection. – J. Atmos. Sci. **60**, 1201–1219.

Sühring, M., S. Raasch, 2013: Heterogeneity-induced heat-flux patterns in the convective boundary layer: Can they be detected from observations and is there a blending height? A large-eddy simulation study for the LITFASS-2003 experiment. – Bound.-Layer Meteor. **148**, 309–331.

Tiedtke, M., 1989: A comprehensive mass flux scheme for cumulus parameterization in large-scale models. – Mon. Wea. Rev. **117**, 1779–1800.

Von Storch, H., F.W. Zwiers, 2001: Statistical analysis in climate research. – Cambridge University Press, 484 pp.

Wicker, L., W.C. Skamarock, 2002: Time-splitting methods for elastic models using forward time schemes. – Mon. Wea. Rev. **130**, 2088–2097.